

An optimal transport model for dynamical shapes, collective motion and cellular aggregates

Antoine DIEZ¹ and Jean FEYDY²

¹Institute for the Advanced Study of Human Biology (ASHBi)
Kyoto University Institute for Advanced Study,
Kyoto University,
Yoshida-Konoe-cho, Sakyo-ku, Kyoto 606-8501, Japan.

²HeKA team, Inria Paris, Inserm, Université Paris-Cité,
PariSanté Campus, 2-10 rue d'Oradour-sur-Glane,
75015 Paris, France

Abstract

Many biological systems such as cell aggregates, tissues or bacterial colonies behave as unconventional systems of particles that are strongly constrained by volume exclusion and shape interactions. Understanding how these constraints lead to macroscopic self-organized structures is a fundamental question in e.g. developmental biology. To this end, various types of computational models have been developed: phase fields, cellular automata, vertex models, level-set, finite element simulations, etc. We introduce a new framework based on optimal transport theory to model particle systems with arbitrary dynamical shapes and deformability. Our method builds upon the pioneering work of Brenier on incompressible fluids and its recent applications to materials science. It lets us specify the shapes of individual cells and supports a wide range of interaction mechanisms, while automatically taking care of the volume exclusion constraint at an affordable numerical cost. We showcase the versatility of this approach by reproducing several classical systems in computational biology. Our Python code is freely available at: www.github.com/antoinediez/ICeShOT

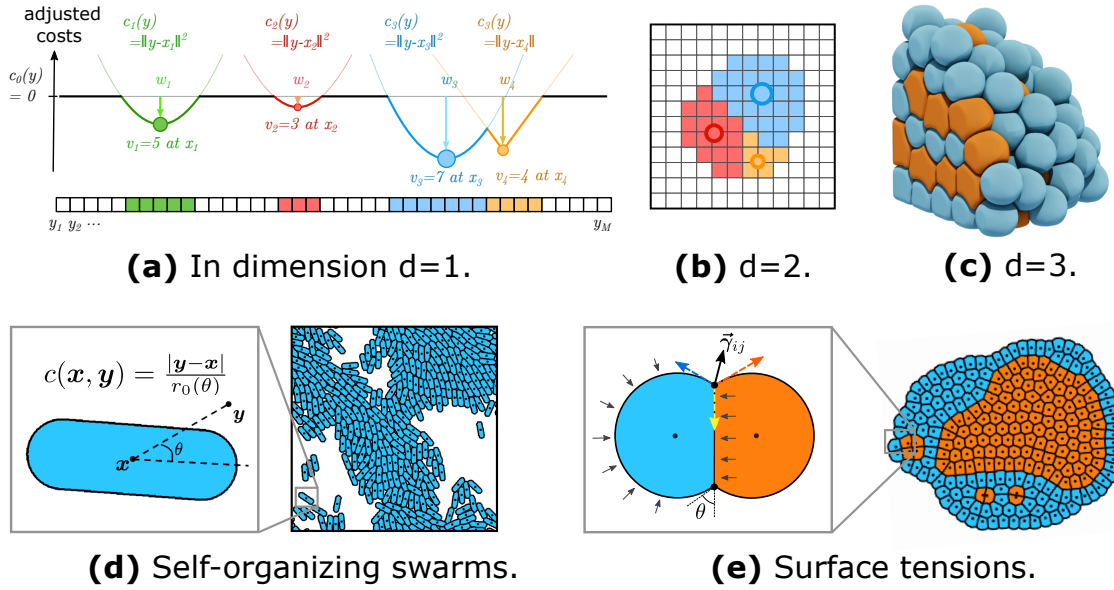


Figure 1: Graphical abstract. (a) We model cells on a domain $\Omega \subset \mathbb{R}^d$ using positive volumes $v_i > 0$ and cost functions $c_i : \mathbf{y} \mapsto c_i(\mathbf{y}) \in \mathbb{R}$ that penalize the assignment of a location \mathbf{y} to the i -th cell. To compute the shapes of a collection of N cells $(v_1, c_1), \dots, (v_N, c_N)$, we rely on a decomposition of the domain Ω into pixels $\mathbf{y}_1, \dots, \mathbf{y}_M$. Then, assigning the points \mathbf{y}_j to their preferred cells corresponds to a discrete optimal transport problem that can be solved efficiently in dimension 2 (b) and 3 (c). Depending on the cost function c_i , a cell may either be hard (c, blue) or soft (c, orange), see also SM Video 24. To model dynamical systems in silico, we alternate between computing cell shapes with optimal transport and updating the cell parameters (v_i, c_i) according to various interaction models. (d-e) Our method is versatile: it supports arbitrary cell shapes and interactions, while automatically taking care of the volume exclusion constraint. Using plain Python code, we show that collective behaviors emerge from interactions between incompressible cell shapes.

Author summary

In complement to conventional experimental studies, mathematical and numerical models can provide more experimental freedom and new insights to study complex biological systems at a negligible cost. In this so-called in silico modelling framework, the goal is to design computer simulations of biological systems, seeking a challenging compromise between physical accuracy, computation speed, versatility and mathematical analysis potential. Over the past years, several models have been designed to target one of these aspects or with specific applications in mind. In the present work, we introduce a new versatile modeling framework to simulate large systems of soft particles with strong mechanical constraints. We demonstrate the applicability of this framework on various classical test cases, with a particular focus on self-organization and collective dynamics

phenomena in cell aggregates. Our model achieves close to state-of-the-art computational performance while keeping a clear analytical mathematical structure. Connections with other old and recent models are also discussed.

1 Introduction

From the smallest intracellular scale [52] to the macroscopic population scale [85], shape, deformations and congestion effects play a central role in the dynamics of biological systems. At the scale of micrometers, cells, bacteria and other microorganisms appear in a wide variety of morphologies. They form dense, dynamical, complex multicellular structures such as epithelial tissue or swarming colonies with a macroscopic behavior [96]. Among other examples: the peculiar shape of some bacteria conditions their collective motion [35, 136]; the membrane deformations of mesenchymal cells induce their migration [129, 127]; the complex viscoelastic properties of cell aggregates induced by cell-cell contact interactions [77, 140, 20] give rise to complex sorting patterns [3, 86] and tissue structures [33, 57, 92, 93, 138, 72]. Crucially, in such crowded systems, the shapes of cells and their varied degrees of deformability strongly constrain global movements and morphological changes [6]. Understanding and measuring these effects is a challenging but important experimental problem, especially in developmental biology [64, 63].

Over the past decades, in complement to *in vitro* and *in vivo* experimental studies, these questions have been studied using mathematical modeling. *In silico* experiments let us assess the impact of conjectured biophysical laws in minimal experimental settings. This poses a modeling and implementation challenge as that there is no unique and simple mathematical way of representing dynamical shapes and multicellular systems. This has motivated the development of various classes of models. In short, the purpose of the present article is to introduce a new approach based on optimal transport theory to construct space tessellations with strict volume constraints. Our framework is particularly versatile and is applicable in most situations encountered in computational biology such as the aforementioned ones.

Before explaining the details and for later comparison, we first briefly review some of the classical approaches. We also refer to [105, 21, 141] and to the introductions of [94, 70] for an in-depth discussion of the different approaches.

- **Enriched point-particle systems.** Extending the core idea of statistical physics, the pioneering work of Vicsek [143] has shown that simple but potentially high-dimensional dynamical systems can accurately describe important collective motion phenomena in biology. In this class of models, one uses a group of active particles to represent migrating cells, microorganism colonies or larger animal societies. Each particle is described by a set of

xyz coordinates coupled with additional basic information variables such as polarity vectors [143, 31], 3D orientation matrices [40] or finite-dimensional shape parameters (size, aspect ratio, etc.) [78, 54]. The formal simplicity of these models can be a drawback, since particles are not detailed enough to represent realistic morphologies. On the other hand, this also makes particle models appealing for both coarse-grained mathematical analysis [29, 27, 144] and large-scale numerical simulations [41, 111].

- **Phase fields, level-sets and boundary flows.** Representing arbitrary shapes requires an infinite-dimensional description. Several techniques can be borrowed from the study of free-boundary and interface problems. For instance, instead of using a single (enriched) point, a cell can be described as a smoothed indicator function of the set that represents its full shape. Using a dynamical Allen-Cahn type motion, this phase-field approach has been applied successfully many times in biology [101, 75, 126, 99]. Strongly connected approaches consider the evolution of the boundary of a shape, defined as a curve [104, 118, 59, 103] or as the level set of some potential function [107, 106, 128, 148, 94, 131].
- **Cellular automata and lattice models.** With a completely different approach, Glazier and Graner [50, 53] introduced the Cellular Potts framework as an extension of lattice models from statistical physics. In this setting, the spatial domain is discretized into a uniform grid lattice with each “pixel” representing either one biological cell or a portion of it. The pixel allocation and flipping dynamics are defined using custom energy minimization rules and implemented via a stochastic Metropolis-type algorithm.
- **Voronoi tessellation.** Historically, cellular arrangement in a tissue were first described as an off-lattice tiling of the space by polygonal shapes [60, 134]. In the classical Voronoi tessellation, each polygonal cell is generated from a seed point (or centroid), that can be interpreted as a cell nucleus, by considering all the spatial points which are closer to this seed point than to any other seed point. This optimization problem is relatively simple to solve and produces sufficiently realistic configurations. Recent experimental observations [71, 92] have motivated the development of refined optimization criteria and detailed interaction mechanisms to model contact forces and locomotion [10, 9] and other complex physical phenomena, see in particular [121] for a hybrid level-set/Voronoi tessellation method. Our approach generalizes this line of work to flexible, non-polygonal shapes.
- **Vertex models, meshes and finite elements.** Unlike Voronoi tessellations for which the centroids are the main degrees of freedom, vertex models define a tiling of the space via a set of vertices connected by straight edges in 2D or plane surfaces in 3D [61]. The motion of each vertex is driven

by a force balance equation that often comes from an energy minimization hypothesis. A detailed mathematical formulation and successful applications to e.g. the epithelial tissue are presented in [2, 125] and references therein. We also mention several recent improvements of the method that build connections with point-particle and Voronoi tessellation models [5, 8] or that consider general edge shapes [65]. Another extension of the vertex model applied to multicellular systems divides each cell into a finite number of subcellular elements, thus creating an effective meshing of the cell membrane, the cell interior and/or the cell environment [83, 117, 142]. This leads to powerful computational approaches originally developed for fluid and fluid-structure interactions, such as the immersed boundary method [109, 67, 116] and the finite element method [32, 139, 149].

Importantly for computational biology, all the methods mentioned above are now available as (mostly) open source software. Among others, we may cite SiSyPHE and PhysiCell for particle and spheroid models [41, 49], MorphoSim for phase-fields [74], Morpheus and CompuCell3D for cellular automata models [132, 135], Tissue Forge for vertex models [125], Chaste [34] for a wide range of cell-based modelling frameworks, OmniverseTM, Interacting Active Surfaces, CellSim3D, PolyHoop, SimuCell3D and Goo for finite elements, mesh-based and physics based models [102, 139, 83, 142, 117, 88]. We also mention cellPACK which solves 3D packing problems with objects of various sizes and shapes for applications to intracellular crowding [68].

Our approach. Be it for cells in multicellular aggregates, microorganisms or pedestrians, the first measurable quantity is the volume. As a starting point, we thus build our method around an independent volume constraint for each cell. This does not mean that volumes cannot evolve in time, but that initial volumes are given as an input of the model and are treated as first-class variables. This contrasts with most of the approaches described above (phase-fields, cellular automata and vertex models), which preserve cell volumes using soft constraints and relaxation forces towards a preferred size. Voronoi tessellation methods do not usually consider a volume constraint, or only provide little control on this quantity [10]. As a first description, our method can be seen as a generalized Voronoi tessellation method which includes strict volume constraints. To achieve this goal, we rely on the notion of Laguerre tessellation which has recently appeared in various different contexts, in particular the simulation of incompressible fluid flows [16, 47, 81], of crowd motion [85, 76] and the modeling of polycrystalline materials [11, 14, 25].

Although all these situations seem quite different, and also quite far from computational biology, they can all be related to the theory of optimal transport. Originally developed for operations research and economics by Monge and Kantorovich, this theory describes the most effective way of allocating resources

(canonically, piles of sand or flour) from one location to another while minimizing a transportation cost that is a function of the distance. We refer to [43, 110, 119, 145, 146] and SM Appendix 4 for classical references. The first connection between optimal transport and fluid mechanics has been made in the pioneering work of Brenier [16, 18, 19]. Classically, the motion of an incompressible fluid is described through macroscopic quantities such as the local density or local speed, which satisfy the Euler or Navier-Stokes equations. Brenier has introduced a Lagrangian description of this motion, i.e. a set of equations which describe the individual motion of fluid particles based on the solution of an optimal transport problem. In the modern implementation of Brenier’s ideas [47, 81], the notion of Laguerre tessellation appears as the natural spatial discretization procedure that preserves the incompressibility constraint, encoded in the volume of the fluid particles. Similar ideas are also used in [85, 76] to model congestion and crowd motion, where volume exclusion also plays a crucial role. More recently, and as a direct inspiration for our work, Laguerre tessellations and their connections with optimal transport have been applied to materials science [1, 11, 14, 25]. Similarly to biological cell aggregates, some materials like steel are made up of a collection of tiny “crystals” with various shapes and sizes. The ability to generate *in silico* structures for an arbitrary set of crystal grains is key to understanding the mechanical properties of several alloys.

On the implementation side, a fundamental insight from the literature is that since the optimal transport problem generalizes sorting to spaces of dimension $d > 1$, it can be solved efficiently using a divide-and-conquer “multiscale” strategy [43, 124, 123, 98, 16]. This idea has been successfully implemented on massively parallel Graphics Processing Units (GPUs), with modern solvers now handling millions of particles in seconds through a convenient Python interface [30, 46]. These computational gains have led to the development of several scalable methods based on optimal transport for e.g. 3D shape registration [44, 130], transcriptomics [122], astrophysics [79], fluid mechanics and computer graphics [37, 47, 81, 112, 113].

Our framework relies extensively on these progresses and lies at the intersection of materials science and computational fluid dynamics. In particular, we show that Laguerre tessellations let us model general shapes: appropriate transport cost functions encode arbitrary deformability properties, in a dynamical setting and with a strict preservation of the volume constraints. Although our model is formally a tessellation model, we show that it shares important properties with particle systems, level-set methods and vertex models, which thus also suggests a novel optimal transport point of view for these methods. As a consequence, our model is remarkably versatile: within the same framework, we can represent individual particles with arbitrary shapes (as in level-set methods), their collective motion (as in point-particle systems) and much denser tissue-like aggregates whose dynamics is ruled by surface tension and other contact-based interactions

(as in vertex and finite elements models).

Remark 1. *Throughout the article, we use the generic word “particle” that, in most cases, will refer to a biological cell. However, our framework is quite general and potentially applicable to other contexts: a particle can also occasionally refer to a bacteria, a pedestrian in a crowd or any general soft body.*

The article is organized as follows. The first section introduces the key notion of Laguerre tessellation in connection with optimal transport in a static framework and presents the implementation and the main components of our model in a dynamical framework. The next three sections are devoted to the results and illustrate the applicability of the model in various situations. The first of these three sections studies soft body systems with arbitrary deformability properties. The two other sections showcase the applicability of our method in two important contexts: first, the collective motion of particles induced by shape deformations due to collisions and external stimuli; and second, the dynamics of multicellular aggregates whose self-organized sorting patterns are induced by surface tension and surface interactions. The last section is devoted to the discussion of these results and the future developments of the model.

The supplementary material has four independent parts. The first section presents technical details on some simulations presented in the main text. Additional numerical experiments, in particular for soft active particles and crowd motion are presented in the second part. The third part investigates mathematically the formal theoretical links between our agent-based framework and new macroscopic continuum PDE models via the notion of mean-field limit. Finally, although the main text of the article is meant to be sufficiently self-contained, the last part gathers reminders on optimal transport theory.

2 Model

2.1 Particles with a volume

Let us consider N particles in a bounded domain $\Omega \subset \mathbb{R}^d$, with positions $\mathcal{X}_N = (x_1, \dots, x_N)$ and volumes denoted by $\mathcal{V}_N = (v_1, \dots, v_N)$. Each particle, generically labelled by $i \in \{1, \dots, N\}$, is therefore not reduced to a point but occupies a certain subset $\mathcal{S}_i \subset \Omega$ of the available space. The position x_i of a particle i should be understood as a positional indication but as we shall see later, it does not necessarily correspond to the barycenter of the set \mathcal{S}_i . It is however directly comparable to the seed or generator point of a Voronoi tessellation.

Throughout this article, we assume that the domain denoted by Ω is connected and bounded, with total volume $|\Omega| = 1$ and typical length $L = 1$. The centroid positions x_i are assumed to be properly adimensionalized with respect to this length scale. The notation $|\cdot|$ denotes indifferently the volume of a set,

understood as its Lebesgue measure, or the Euclidean norm of a vector. Then we make the following two assumptions.

- **Non-overlapping:** the sets \mathcal{S}_i are disjoint.
- **Incompressibility:** the volume of each particle is fixed $|\mathcal{S}_i| = v_i$.

Naturally, these constraints imply that the particles need to adapt their shapes to their current environment, especially in crowded and dynamical situations. The main contribution of the present work is to introduce a new way of computing optimal shapes depending on the current configuration and on the individual deformability properties of the particles.

From a mathematical point of view, we are looking for a partition of the space $\Omega = \cup \mathcal{S}_i$ into disjoint components with given volumes $|\mathcal{S}_i| = v_i$ and we denote by $V = v_1 + \dots + v_N$ the total volume that is occupied by the cells. When cells form a tissue, it is natural to expect that $V = 1$: the particles fill all the available space. In other situations, there may be some free space between the particles and $V < 1$: for instance when cells are migrating in a medium. In this case, the extra-space will be seen as one additional component of the partition of the space, i.e. we add one additional particle with volume $1 - V$. Another approach would be to discretize this free space into a certain number of extra particles each with a very small volume compared to the v_i 's. In our framework, both approaches are actually equivalent as shown in [81]. Using the first method with a single big particle is much more efficient numerically; on the other hand, discretizing the medium with tiny particles lets us model a fluid behavior that may be relevant in some settings.

2.2 Static framework

2.2.1 Semi-discrete optimal transport framework

Two important classes of off-lattice models for multicellular systems use the same idea of building a partition of the space. First, vertex models define a partition through an arbitrary number of vertices and edges that create a meshing of the space. Second, (generalized) Voronoi diagrams construct a partition by solving an optimization problem to assign each point of the space to one of several “seed” points. As we explain below, our framework extends this class of models by casting such an optimization procedure as an optimal transport problem.

A partition of the space that satisfies the incompressibility constraint can be seen as a map $T : \Omega \rightarrow \{x_i\}_i$ (or more generally $T : \Omega \rightarrow \Omega$) that satisfies the volume constraint $|\mathcal{S}_i| = v_i$ where $\mathcal{S}_i := T^{-1}(\{x_i\})$ is the set of points in Ω that are sent to x_i by T . We call such a map a partition map. A simple but remarkable property, which is the basis of our work, is that a partition map can also be understood as the solution of a semi-discrete transport problem. First,

let us state the following lemma – reminders about measure theory and optimal transport are gathered in SM Appendix 4:

Lemma 2. *Let $\hat{\mu} = \sum_{i=1}^N v_i \delta_{x_i}$ be a discrete measure with weight v_i at location x_i . Then a map $T : \Omega \rightarrow \Omega$ is a partition map if and only if $T\#\text{Leb} = \hat{\mu}$, i.e. if it pushes the Lebesgue measure of Ω onto $\hat{\mu}$.*

Proof. For a given bounded continuous function $\phi \in C_b(\Omega)$, we recall the definition of the push-forward measure $T\#\text{Leb}$,

$$\int_{\Omega} \phi(x) T\#\text{Leb}(dx) = \int_{\Omega} \phi(T(x)) dx.$$

Thus, if T is a partition map, its image set is the discrete set $\{x_i\}_i$ so

$$\int_{\Omega} \phi(x) T\#\text{Leb}(dx) = \sum_{i=1}^N \phi(x_i) |T^{-1}(\{x_i\})| = \sum_{i=1}^N v_i \phi(x_i) = \int_{\Omega} \phi(x) \hat{\mu}(dx).$$

Conversely, if $T\#\text{Leb} = \hat{\mu}$ then by choosing a test function whose support does not contain any x_i , one can see that the image set of T is contained in $\{x_i\}_i$. Then, for any i and using the same formula as above, by choosing a test function ϕ which is equal to one on x_i and 0 on all the other x_j , it is easily checked that $|T^{-1}(\{x_i\})| = v_i$. \square

Without further hypothesis, there exists an infinite number of partitions of the space. With the previous measure transportation formulation in mind, we consider the partition map that is solution of the ‘‘Monge’’ optimization problem from optimal transport theory. We assume that allocating each point of $T^{-1}(\{x_i\})$ to x_i has a certain cost and we are looking for the minimal total allocation cost:

$$\min_{\substack{T: \Omega \rightarrow \Omega \\ T\#\text{Leb} = \hat{\mu}}} \sum_{i=1}^N \int_{T^{-1}(\{x_i\})} c(x, x_i) dx, \quad (1)$$

where the function $c : \Omega \times \{x_i\}_i \rightarrow [0, +\infty)$ is called the cost function. Provided that this optimization problem has a unique solution for a given cost, this provides an arbitrary but clearly defined way of computing a partition of the space. As shown in the following theorem, it is well known that the semi-discrete Monge problem (1) has a unique solution under mild hypotheses on the cost function.

Theorem 3. *Let $\hat{\mu} = \sum_{i=1}^N v_i \delta_{x_i}$ be a discrete probability measure on Ω . Let c be a cost function such that for all i , $c_i : x \in \Omega \mapsto c(x, x_i) \in [0, +\infty)$ belongs to $C^{1,1}(\Omega)$ and $y \mapsto \nabla_x c(x, y)$ is injective for all $x \in \Omega$. Then the Monge problem (1) has a unique solution T given by*

$$T : \Omega \rightarrow \{x_i\}_i, \quad x \in \mathcal{L}_i \mapsto x_i$$

where the partitioning sets $(\mathcal{L}_i)_i$ are the (generalized) Laguerre cells defined by

$$\mathcal{L}_i := \{x \in \Omega : c(x, \mathbf{x}_i) - w_i \leq c(x, \mathbf{x}_j) - w_j \ \forall j\}. \quad (2)$$

The intersection of two Laguerre cells has zero Lebesgue measure and the weights $w_i \in \mathbb{R}$, called Kantorovich potentials, are uniquely defined such that for all $i \in \{1, \dots, N\}$,

$$|\mathcal{L}_i| = v_i. \quad (3)$$

Optimal transport solvers are computer programs that take as input the weights v_1, \dots, v_N , the cost functions c_1, \dots, c_N , and return as output the unique vector of optimal values for the Kantorovich potentials (w_1, \dots, w_N) .

This result is well-known and proved for instance in [13, 73] (see also SM Appendix 4 for more details) where it is applied to computational fluid dynamics and materials science problems. To the best of our knowledge, it is the first time that this result is used for biological applications. In particular, although the result is valid for very general cost functions, most applications consider the L^2 cost function (or variations of it):

$$c(x, \mathbf{y}) = |\mathbf{y} - x|^2. \quad (4)$$

One of the main focus of the present work is to investigate how the choice of an appropriate cost function lets us model various biophysical properties and behaviors. As a first static example, Fig. 2 shows three examples of a tessellation of a square periodic domain obtained by Theorem 3 with different cost functions and different particles shapes.

Remark 4 (Scaling). Given a cost c , one can define the energy of a partition $\mathcal{S} = (\mathcal{S}_i)$ of Ω by

$$\mathcal{E}(\mathcal{S}) := \sum_i \int_{\mathcal{S}_i} c(x, \mathbf{x}_i) dx. \quad (5)$$

Theorem 3 shows that for a given set of points \mathbf{x}_i and volumes v_i , the lowest energy is the transport cost between the Lebesgue measure and the discrete empirical measure $\hat{\mu}$:

$$\mathcal{T}_c(\hat{\mu}) = \min_{\substack{\cup \mathcal{S}_i = \Omega \\ |\mathcal{S}_i| = v_i}} \mathcal{E}(\mathcal{S}).$$

With this remark in mind, a natural scaling for the cost is to impose a finite energy to a base shape. Unless otherwise specified, for better numerical stability, the cost $c(x, \mathbf{x}_i)$ will always be rescaled so that, given a dimensionless scaling parameter $\lambda_i > 0$ and a base shape \mathcal{S}_0 with volume V_0 ,

$$\int_{\mathcal{S}_0} c(x, \mathbf{x}_i) dx = \lambda_i V_0. \quad (6)$$

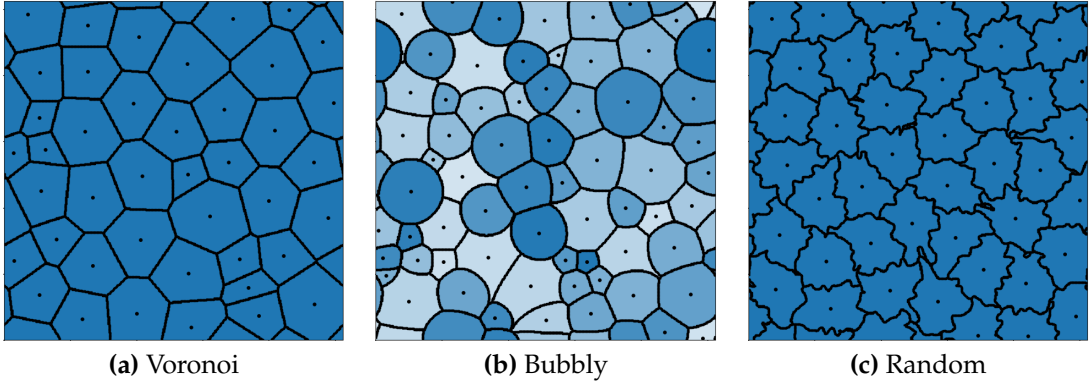


Figure 2: (a) A Voronoi tessellation obtained with the L^2 cost of Eq. (4) and 42 particles with random volumes v_i sampled uniformly between 0.2 and 1 (before normalization to sum up to 1). (b) A bubbly tessellation similar to [65] obtained for 66 particles with random volumes sampled uniformly between 0.05 and 1 (before normalization) and a power cost $c(x, x_i) = |x - x_i|^{\alpha_i}$ where the α_i are distributed uniformly between 0.5 and 4. Lighter colors indicate lower values of α_i and correspond to softer shapes. (c) A Voronoi tessellation with random fluctuations similar to [92] obtained with 42 identical particles and a randomly perturbed L^2 cost as explained in a forthcoming section.

2.2.2 Laguerre tessellation as generalized Voronoi diagrams with volume constraints

The Laguerre tessellation of the space given by the sets (2) is reminiscent of the notion of generalized Voronoi cells defined by

$$\mathcal{V}_i = \{x \in \Omega, d(x, x_i) < d(x, x_j) \forall j\},$$

where d is an arbitrary generalized distance function. In a classical Voronoi tessellation, the function d is equal to the Euclidean distance $d(x, x_i) = |x - x_i|$ and the resulting Voronoi cells are convex polytopes. For biological applications, this is not always realistic [71], as cell aggregates sometimes exhibit curved boundaries, possibly even with random fluctuations [92] (as in Fig. 2). Following this remark, some motivating examples for the concept of generalized Voronoi diagram are discussed in particular in [10, 65, 57] and in the references therein. Replacing the Euclidean distance by an arbitrary function d indeed naturally allows other boundary shapes, and in particular circular arcs, a topic which is discussed in details in [10] using the generalized distance functions

$$d(x, x_i) = |x - x_i|^2 - s_i^2, \quad d(x, x_i) = |x - x_i|^2 / s_i^2, \quad (7)$$

where $s_i \in \mathbb{R}$ is a tunable scaling parameter.

Formally, the Laguerre cells defined by Eq. (2) could be seen as generalized Voronoi cells with the generalized distance function $d(x, x_i) = c(x, x_i) - w_i$. Since,

at this point, the cost function c is as arbitrary as the generalized distance function d , in comparison to the introduction of [10], this discussion is mostly about naming conventions. However, more importantly, our optimal transport perspective provides an original point of view on the three following topics.

1. The Laguerre cells in Theorem 3 are generalized Voronoi cells that satisfy the strict volume constraints Eq. (3) thanks to an optimal choice of the Kantorovich potentials w_i . Note that in [10], the scaling parameter s_i in the definition of generalized distances is also introduced as a way of controlling the size of the particles – but without a formal link to strict volume constraints. Since volume is often the first experimentally measurable quantity, it is desirable to include it as an easily controllable degree of freedom of the model.
2. While most of the literature in computational geometry focuses on the square Euclidean cost (as in [10]), the optimal transport interpretation naturally suggests other choices that we investigate below. As shown in the result sections, this lets us encompass both tissue-like aggregates (for which generalized Voronoi tessellations are commonly accepted as accurate models) and individual particles with arbitrary deformable shapes (which are often modeled using completely different methods).
3. The numerical computation of (generalized) Voronoi tessellations is a classical but non-trivial problem in computational geometry. Based on the optimal transport interpretation, we propose an alternative and novel numerical method that is applicable to arbitrary cost functions.

2.2.3 Laguerre cells as sublevel sets

As mentioned in the introduction, when the particles do not fill the entire space, a simple strategy is to add an additional particle labelled by $i = 0$ with volume $v_0 = 1 - \sum_{i \geq 1} v_i$ at an arbitrary position $x_0 \in \Omega$. The exact position of this particle will not matter as it will be associated to the cost $c(x, x_0) = 0$ for all $x \in \Omega$. With this choice, we may consider individual isolated particles that only share a boundary with the surrounding medium modeled by the particle x_0 . A direct corollary of Theorem 3 shows that the shape of an individual particle is always a sublevel set of the cost function.

Lemma 5. *The shape $\mathcal{S} \subset \Omega$ that minimizes the individual energy*

$$\mathcal{I}(\mathcal{S}) = \int_{\mathcal{S}} c(x, x_i) dx$$

is of the form

$$\mathcal{S}(w) = \{x \in \Omega, c(x, x_i) \leq w\},$$

for some potential $w > 0$.

Note that with the notations of Theorem 3, one can write more precisely the potential w as the difference between the Kantorovich potentials $w = w_0 - w_i$. Since this is an important property, we provide a direct self-contained proof.

Proof. First of all, since the function $U : w \mapsto |\mathcal{S}(w)|$ is non-decreasing, $U(0) = 0$ and $U(w) \rightarrow 1$ as $w \rightarrow +\infty$ there exists a unique $w^* > 0$ such that $U(w^*) = v_i$. Then let $\mathcal{S} \subset \Omega$ be any shape of volume v_i . Denoting $\mathcal{S}^* = \mathcal{S}(w^*)$, it holds that

$$\begin{aligned} \mathcal{I}(\mathcal{S}) &= \mathcal{I}(\mathcal{S} \cap \mathcal{S}^*) + \mathcal{I}(\mathcal{S} \cap (\mathcal{S}^*)^c) \\ &= \mathcal{I}(\mathcal{S}^*) + \mathcal{I}(\mathcal{S} \cap (\mathcal{S}^*)^c) - \mathcal{I}(\mathcal{S}^* \cap \mathcal{S}^c) \end{aligned}$$

By assumption $|\mathcal{S}^*| = |\mathcal{S}| = v_i$ so it holds that

$$|\mathcal{S} \cap (\mathcal{S}^*)^c| = |\mathcal{S}^* \cap \mathcal{S}^c| =: \tilde{v}_i \geq 0,$$

and by definition of \mathcal{S}^* ,

$$\mathcal{I}(\mathcal{S} \cap (\mathcal{S}^*)^c) \geq \tilde{v}_i w^*, \quad \mathcal{I}(\mathcal{S}^* \cap \mathcal{S}^c) \leq \tilde{v}_i w^*,$$

which gives

$$\mathcal{I}(\mathcal{S}) \geq \mathcal{I}(\mathcal{S}^*).$$

□

These potentials are analogous to the signed distance functions that are commonly used for volumetric rendering in computer graphics [114] – with the added benefit that the derivative of our cost encodes the local deformability of the shape as shown later. Consequently, any particle shape can be realized using an appropriate cost function $c_i : \mathbf{x} \in \Omega \mapsto c(\mathbf{x}, \mathbf{x}_i) \in [0, +\infty)$. For instance, in dimension 2, any shape defined by a polar equation $r = r_0(\theta)$ can be encoded by the cost

$$c(\mathbf{x}, \mathbf{x}_i) = \left(\frac{|\mathbf{x} - \mathbf{x}_i|}{r_0(\theta(\mathbf{x}, \mathbf{x}_i))} \right)^p, \quad (8)$$

where $\theta(\mathbf{x}, \mathbf{x}_i)$ denotes the polar angle of the vector $\mathbf{x} - \mathbf{x}_i$ and $p > 0$ is a hardness parameter whose influence is illustrated in Figs 2 and 7. Indeed, all the sublevel sets of the function (8) are scaled version of the base shape $r = r_0(\theta)$, and the only one with the correct volume is automatically selected by the Kantorovich potential w in Lemma 5. Note that other cost functions could be considered, as long as the desired shape is a sublevel set.

Remark 6. For any exponent p , this cost satisfies the scaling (6) with $\lambda_i = 2/(p + 2)$ and the base shape \mathcal{S}_0 , the boundary of which is defined by the polar equation $r = r_0(\theta)$. This construction extends to any dimension d when r_0 defines the equation of a closed $(d - 1)$ -dimensional surface (in which case $\lambda_i = d/(p + d)$).

Representing individual particles with arbitrary shapes as sublevel sets of some custom functions is a well-known method in computational biology, see for instance [148, 94]. Although this idea appears naturally in our framework, it should be noted that it formally comes from a partition of the space and not from an interface tracking method as in traditional sublevel set methods [148, 94]. This has a clear advantage since when two particles are in contact, there is no particular surgery to consider when computing their contact surface which is simply the intersection of two Laguerre cells

$$\mathcal{L}_i \cap \mathcal{L}_j \subset \{x \in \Omega, c(x, x_i) - w_i = c(x, x_j) - w_j\}.$$

Consequently, our framework handles well individual particles, dense tissue-like aggregates with topological connectivity changes, or a mix of both.

2.3 Implementation

The pioneering work of Brenier [16, 18, 19] on the connection between optimal transport and incompressible fluid flows motivated the development of fast and efficient numerical methods to compute Laguerre tessellations, with remarkable achievements in computational fluid dynamics [47, 81, 37] and more recently in material science [1, 11, 14].

Whether it is in computational fluid dynamics or in materials science, the semi-discrete optimal transport problem is considered mostly for the squared Euclidean cost $c(x, y) = |x - y|^2$. Extremely efficient numerical methods, based on a damped Newton algorithm, have been developed for this case and are now available as open source softwares [80, 12, 89, 91]. Unfortunately, these implementations leverage the structure of the squared Euclidean distance to compute Laguerre cells efficiently [115] and cannot be applied with general cost functions.

This prevents us from using them for biological applications: the freedom in the choice of arbitrary, individualized cost functions c_i is of utmost importance to our approach. To unlock the use of Laguerre cells with general shapes and deformability properties, we work in a fully discrete setting with a discrete approximation of the Lebesgue measure

$$\hat{\mu}_0 = \frac{1}{M} \sum_{j=1}^M \delta_{y_j} \approx \text{Leb},$$

that is supported by “pixel centers” y_j on a uniform grid discretization of the space $\Omega = [0, 1]^d$ (as shown in Fig. 1(a)-(b)). We choose $M \gg N$ so that each particle is effectively discretized with a sufficiently high number of pixels y_j with volume $1/M$. Solving discrete optimal transport problems is by now classical owing to numerous applications in data science [110]. A quite reliable and stable method is the symmetrized and annealed variant of the renowned Sinkhorn

algorithm [43, Algorithm 3.5]. However, as we target a tight fit to the volume constraints and work in a dynamical setting that lets us re-use optimal potential values w_i from one time step to another, we rely instead on a solver that leverages the semi-discrete structure of the problem. The main observation, proved for instance in [13, 147], is that the dual potentials $w = (w_i)_{i=1,\dots,N}$ that appear in the definition Eq. (2) of the Laguerre cells solve the dual maximization problem

$$w = \arg \max_{(w_i)_{i=1,\dots,N}} \mathcal{K}(w), \quad \mathcal{K}(w) := \sum_{i=1}^N v_i w_i + \int_{\mathbf{y} \in \Omega} \min_{i=1,\dots,N} [c(\mathbf{y}, \mathbf{x}_i) - w_i] d\mathbf{y}.$$

The objective $\mathcal{K}(w)$ is concave as the sum and minimum of functions that are linear with respect to w . Its gradient simply reads

$$\nabla \mathcal{K}(w) = (v_i - |\mathcal{L}_i|)_{i=1,\dots,N}$$

where \mathcal{L}_i is defined by Eq. (2) for an arbitrary set of potentials. This implies that the optimality conditions $|\mathcal{L}_i| = v_i$ are satisfied at the maximum of \mathcal{K} , which is well-defined if the sum of the target volumes v_i does not exceed that of the domain Ω and if the cost functions $c_i : \mathbf{y} \mapsto c(\mathbf{y}, \mathbf{x}_i)$ satisfy mild technical assumptions: notably, distinct indices $i \neq j$ should correspond to distinct cost functions $c_i \neq c_j$.

In order to solve this maximization problem, we follow [25] and rely on a classical quasi-Newton method, namely the L-BFGS-B algorithm. In a discretized domain $\Omega = \{\mathbf{y}_1, \dots, \mathbf{y}_M\}$ with M large, the most expensive part of the computation of the objective function is the minimum operation over the i -indices of the $N \times M$ matrix $(c(\mathbf{y}_j, \mathbf{x}_i) - w_i)_{i,j}$ followed by a sum over the j -indices approximating the integral. In order to handle arbitrary cost functions and fine discretizations with $M \sim 10^6$ pixels, we rely on the semi-symbolic lazy tensor framework introduced by the KeOps and GeomLoss libraries [30, 46, 45]. This lets our plain Python code perform scalable geometric computations on the GPU, with automatic differentiation and without memory overflows.

A drawback of our discretization procedure is that there is generally no Monge map between two discrete measures (as explained in SM Appendix 4). As a replacement for the Monge map defined in Theorem 3, we thus consider the following discrete allocation map

$$T : \{\mathbf{y}_j\}_{j \in \{1,\dots,M\}} \rightarrow \{\mathbf{x}_i\}_{i \in \{1,\dots,N\}}, \quad \mathbf{y}_j \mapsto \mathbf{x}_{j^*}, \quad (9)$$

with

$$j^* := \arg \min_{i \in \{1,\dots,N\}} \{c(\mathbf{y}_j, \mathbf{x}_i) - w_i\}. \quad (10)$$

Other choices such as the popular barycentric mapping [110, Remark 4.11] could also be considered, but the definition (9)-(10) directly extends that of Theorem 3 and provides the best results in practice.

We use NumPy, PyTorch, KeOps and GeomLoss for our simulations [56, 108, 30, 45, 43] while relying on Matplotlib, PyVista and Paraview for visualizations [62, 133, 4]. Our source code, including an API and the scripts and detailed parameter sets to reproduce all of our numerical experiments, is freely available on GitHub at

<https://github.com/antoinediez/ICeSh0T>

and on the documentation website

<https://iceshot.readthedocs.io/>

2.4 Dynamical setting

As discussed above, Theorem 3 shows that under mild conditions on the cost function, for any positions of the centroids x_i and volumes v_i , there is always a unique optimal partition of the space that satisfies the volume constraint. In a dynamical setting, at each discrete time step, we apply forces to the centroid positions x_i and compute a new Laguerre tessellation of the space. We can also update the volumes and/or the cost functions to model morphological changes, or to include other events such as the creation or deletion of particles. Just as with generalized Voronoi models [9], most of our simulation time is spent updating the space tessellation at each time step. However, thanks to the GPU implementation that is discussed above, this typically takes at most a few seconds, allowing nearly real-time simulations in most situations.

2.4.1 Damped Lloyd algorithm and equations of motion

In a dynamical framework, a reasonable assumption is that, in the absence of other forces, each particle should relax towards its preferred shape, computed by Lemma 5 as a sublevel set of the cost $c_i : \mathbf{y} \mapsto c(\mathbf{y}, x_i)$. In the formula Eq. (5) of the energy of a partition, each term has an absolute minimum when \mathcal{S}_i is the shape given by Lemma 5, i.e. when each particle is only in contact with the medium associated to the zero cost. Consequently, for the whole particle system, the most stable centroid configuration x_1, \dots, x_N is the one that minimizes the total transportation cost

$$\min_{x_1, \dots, x_N} \mathcal{T}_c(\hat{\mu}).$$

As a consequence, we propose the following gradient descent motion for each particle:

$$\dot{x}_i = -\tau_i \nabla_{x_i} \mathcal{T}_c(\hat{\mu}). \quad (11)$$

The gradient descent step $\tau_i > 0$ may vary between particles. We interpret it as an inertia parameter (typically the inverse of a mass) that specifies how easily a particle may be displaced from its current location.

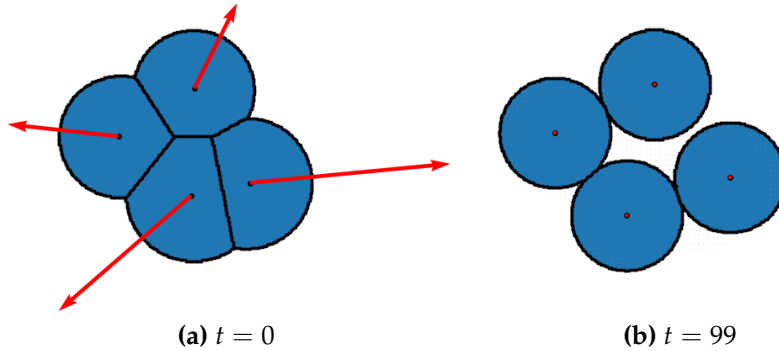


Figure 3: (a) A four-cell configuration showing the incompressibility forces acting on the centroids (red arrows) for the L^2 cost. (b) Equilibrium configuration after 99 Euler discretization steps ($\Delta t = 0.1$) of Eq. (11). See also SM Video 1

Remark 7. As customary in computational biology, we assume that particles evolve in an over-damped regime and only consider first order equations.

The force on the right-hand side of Eq. (11) can also be understood as a repulsion force between the particles (see Fig. 3 and SM Video 1). However, this force strongly differs from the classical repulsion forces in point particle systems, which are typically modeled through a sum of binary interactions

$$\dot{\mathbf{x}}_i = -\tau_i \nabla_{\mathbf{x}_i} \sum_{j=1}^N V(\mathbf{x}_j - \mathbf{x}_i),$$

where V is a repulsive potential. Contrary to this repulsion force, the gradient descent Eq (11) takes into account the shapes and the global configuration of the system. In computational fluid dynamics [47], the gradient of the transport cost can be directly related to the pressure gradient in an incompressible flow. We will thus refer to $-\nabla_{\mathbf{x}_i} \mathcal{T}_c(\hat{\mu})$ as an *incompressibility force*.

On the practical side, it has been shown in [147] that the gradient of the total transport cost has a simple computable expression, namely

$$\nabla_{\mathbf{x}_i} \mathcal{T}_c(\hat{\mu}) = \int_{\mathcal{L}_i} \nabla_{\mathbf{x}_i} c(\mathbf{x}_i, \mathbf{x}) d\mathbf{x}. \quad (12)$$

In particular, when $c(\mathbf{x}, \mathbf{y}) = \ell(|\mathbf{y} - \mathbf{x}|)$ is an isotropic cost which depends only on the distance through a function $\ell : [0, +\infty) \rightarrow [0, +\infty)$,

$$\nabla_{\mathbf{x}_i} \mathcal{T}_c(\hat{\mu}) = \int_{\mathcal{L}_i} \frac{\ell'(|\mathbf{x} - \mathbf{x}_i|)}{|\mathbf{x} - \mathbf{x}_i|} (\mathbf{x}_i - \mathbf{x}) d\mathbf{x}.$$

It is a force in the direction of the weighted barycenter $\bar{\mathbf{x}}_i$ of the Laguerre cell

$$\bar{\mathbf{x}}_i := \frac{\int_{\mathcal{L}_i} \frac{\ell'(|\mathbf{x} - \mathbf{x}_i|)}{|\mathbf{x} - \mathbf{x}_i|} \mathbf{x} d\mathbf{x}}{\int_{\mathcal{L}_i} \frac{\ell'(|\mathbf{x} - \mathbf{x}_i|)}{|\mathbf{x} - \mathbf{x}_i|} d\mathbf{x}}. \quad (13)$$

Note the \bar{x}_i is the actual barycenter of the Laguerre cell when $\ell(r) = \frac{1}{2}r^2$. In computational geometry, the gradient descent Eq. (11) is interpreted as a damped Lloyd algorithm [147, 90] with damping parameter τ_i . In comparison, the classical Lloyd algorithm is an iterative algorithm commonly used to compute well-shaped Voronoi tessellations by repositioning at each iteration the centroids x_i at the barycenter \bar{x}_i . In other words, Lloyd algorithm is the explicit Euler discretization of Eq. (11) with $\tau_i^{-1} = \int_{\mathcal{L}_i(w)} \frac{\ell'(|x-x_i|)}{|x-x_i|} dx$ and a unit time step $\Delta t = 1$.

Although we will typically use Lloyd algorithm to compute realistic initial configurations, the damped version Eq. (11) is preferable as it can be advantageously coupled with additional force or noise terms. The following general mean-field like stochastic differential equation system constitute the basic equations of motion in our model:

$$dx_i = \mathbf{b}(x_i, \hat{\mu})dt - \tau_i \nabla_{x_i} \mathcal{T}_c(\hat{\mu})dt + \sqrt{2\sigma_i} dB_t^i, \quad (14)$$

where \mathbf{b} is a force term which may include interactions with the other particles through $\hat{\mu}$ (and more generally on the whole current Laguerre tessellation $(\mathcal{L}_i)_i$), B_t^i is a Brownian motion and $\sigma_i \geq 0$ is a diffusion coefficient. In other words, the incompressibility force that takes into account the shape of the particles and the global configuration can be added to any point-particle dynamical system. Note that the cost function c in this equation can also depend on time: it will typically evolve depending on the geometrical properties of the system, as explained in the following. In the rest of this article, the dynamics of the system will always be described by a system of (stochastic) differential equations of the form Eq. (14) or a variation of it. For the sake of simplicity, our integration scheme is always a forward Euler method with a step size denoted by Δt . The natural question of the mean-field limit when $N \rightarrow +\infty$ is shortly discussed in SM Appendix 3.

Remark 8 (Boundary conditions). *By definition, the Laguerre cells are always contained in Ω and no particular procedure needs to be considered to handle boundary conditions, which allows arbitrary domain shapes as shown in Fig. 4 and SM Video 26 for a hourglass-like domain and in SM Video 2 for a disk domain. Periodic boundary conditions can also be enforced by replacing every instance of the Euclidean distance $|\cdot|$ by the periodized version d_P along each dimension. For $\Omega = [0, 1]^d$ with periodic boundaries,*

$$d_P(\mathbf{x}, \mathbf{y})^2 := \sum_{k=1}^d \delta_P(x_k, y_k)^2,$$

where $\mathbf{x} = (x_1, \dots, x_d)^T$ and for two scalar values $x, y \in [0, 1]$,

$$\delta_P(x, y) := \min(|y - x|, 1 - |y - x|).$$

No particular constraint is imposed on the centroids x_i . Actually, Theorem 3 remains valid even if $x_i \notin \Omega$, and it does not even imply that $x_i \in \mathcal{L}_i$ either. Nevertheless, this

property holds in all of our experiments thanks to the incompressibility force that tends to reposition the centroids at the (weighted) barycenters of their Laguerre cells. This intrinsic flexibility of our model lets us update the x_i 's without having to worry about hard constraints.

2.4.2 Choosing the cost function and computing the forces: implementing biophysical properties

In the basic equations of motion Eq. (14) the two main modeling choices are the cost function c and the force term \mathbf{b} . For both, our framework allows them to depend (dynamically) on the geometric properties of the Laguerre tessellation. Extracting the relevant information from the Laguerre cells and translating it into biophysical properties and forces is the key modeling choice that defines the behavior of our simulations. In the following three result sections, we will extensively detail three main ideas along these lines, which constitute the core contribution of the present article.

1. The cost function is directly linked to the softness (or deformability) properties of each particle through the steepness of its gradient. In combination with the inertia parameter of the incompressibility force, it allows the simulation of arbitrarily soft, hard, light, heavy or mixed particles in an external force field.
2. Anisotropic shapes or local deformations (such as protrusions) can be implemented by considering general cost functions of the form Eq. (8). In such situation, the cost function typically depends on a set of parameters defining an orientation (polarity, covariance matrix. . .) or some directional bias. These parameters can evolve in time to model the collective motion of particles with a complex oriented structure, while volume exclusion is automatically handled by the incompressibility force.
3. The interaction forces may depend on the contact surface between the Laguerre cells: we consider particles as immersed bodies and apply on the centroids the resulting pressure forces computed along the contact surface. This lets us model surface tension phenomena in cellular aggregates.

For simplicity and clarity, the results will be presented in a two dimensional framework, although most of our modeling framework is independent of the dimension. However, to showcase the method, we first present a few simple illustrative examples in a three-dimensional setting.

2.5 First examples and benchmarks

As a first illustrative example, we consider in Fig. 4 and SM Video 26 a system of falling soft spheres in a hourglass domain with a large spherical obstacle at the

exit of the funnel. The only components in the equations of motion Eq. (14) are a downward constant force \mathbf{b} and the incompressibility force (11) associated to the cost $c(\mathbf{x}, \mathbf{y}) = |\mathbf{y} - \mathbf{x}|^2$.

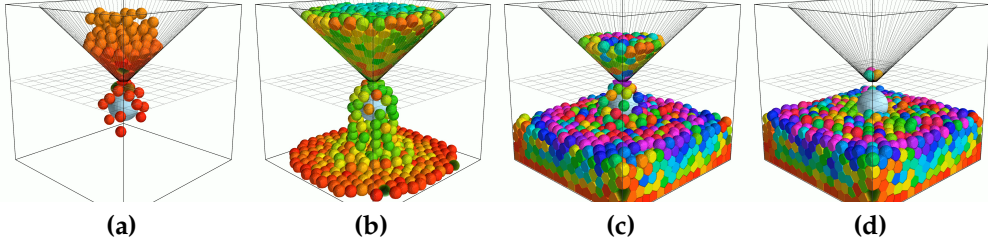


Figure 4: Falling soft-spheres in a hourglass domain. See also Supplementary Video 26.

In order to assess the computational performance of our method, we present two benchmark experiments. The detailed parameters of these experiments can be found in SM 1. All the simulations presented in this article run on a Nvidia RTX A6000 GPU card. At each time step, the stopping criterion for the optimization algorithm is when the average volume deviation (between the computed volumes and the theoretical volumes) falls below 1%. Except for rare isolated events, this is always the case in all the experiments presented.

First, we consider a simple but realistic 3D system of self-propelled deformable ellipsoids in a strongly packed configuration. Each particle moves in the direction of its principal axis which evolves according to a re-orientation process subject to the deformations caused by the surrounding particles. We consider N particles in a 3D bounded box, discretized on a grid of size M^3 . The results are shown in Fig 5 and SM Video 27. The simulation times are presented in the Table 1 below for various values of N and M . Note that we have excluded the cases where the total number of grid cells to fill the volume of the smallest particle is below 100. As expected, the computation times grows linearly with respect to both N and M . For the 2D experiments in the coming sections, we typically use a grid of size 512×512 so the computation times are directly comparable to the case $M = 64$ in the present 3D benchmark: they typically do not exceed a few minutes although they may be affected by the complexity of the cost function or on the operations to compute interaction forces. Note also that GPU computations are sub-optimal for a too small number of particles (under a few dozens).

Secondly, as another classical benchmarking experiment, we consider a 3D cell aggregate growing according to a basic somatic cell cycle [101, 42, 5, 70]. Starting from $N = 1$ cell, each cell grows at a linear speed until a target volume is reached, then it divides after a random exponential time producing two daughter cells with identical half volumes. We stop the simulation when $N = 50,000$ cells fill the entire domain (a fixed bounded box). The result is shown in Fig. 6 and SM Video 28. The entire simulation takes about a day using a constant grid-size

$N \backslash M$	64	128	256	512
10	30 s	1.3 min	7.4 min	62 min
100	45 s	1 min	4.7 min	36 min
1000	NR	4 min	25 min	3 h
10000	NR	NR	4.9 h	35 h

Table 1: Total computation time for 2000 iterations and various values of N and M .

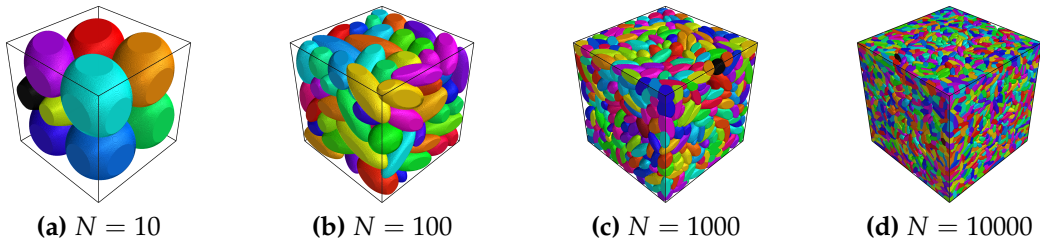


Figure 5: Final configuration of N deformable ellipsoids with $M = 512$. See also SM Video 27.

resolution $M = 400$ and about 2500 time steps, which is comparable to state-of-the-art performance obtained with a mesh-based algorithm [117] (although using a more powerful GPU hardware framework).

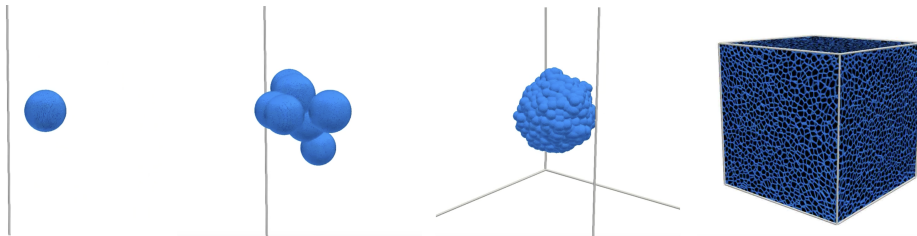


Figure 6: Growth of a 3D aggregate, zooming out from $N = 1$ to $N = 50,000$ cells. See also SM Video 28.

3 Incompressibility force and deformation cost

3.1 Setting

In this section, we illustrate the role of the incompressibility force for different choices of cost functions. We show that the main factor that influences the deformability of a Laguerre cell in our model is the steepness of the cost function $c_i : \mathbf{y} \mapsto c(\mathbf{y}, \mathbf{x}_i)$ along the boundary of the sublevel set of volume v_i , as measured

by the norm of the gradient $|\nabla_{\mathbf{y}}c(\mathbf{y}, \mathbf{x}_i)|$. Large values correspond to hard cells, while small values correspond to soft cells. In order to assess this influence in the gradient descent motion Eq. (11), let us consider the family of isotropic power costs of the form

$$c(\mathbf{y}, \mathbf{x}) = \lambda_{\alpha}^{-1}|\mathbf{y} - \mathbf{x}|^{\alpha} \quad (15)$$

with parameters $\alpha, \lambda_{\alpha} > 0$. For any value of the parameter α , the base shape of the particles is always a ball. In the experiments below, we assume that all the particles have equal volumes $v_i = v_0 = \pi R_0^2$ for a given $R_0 > 0$ (in dimension 2) and we set the scaling parameter $\lambda_{\alpha} = \frac{2}{\alpha+2}R_0^{\alpha}$ so that for any α ,

$$\int_{B(\mathbf{x}_i, R_0)} c(\mathbf{y}, \mathbf{x}_i) d\mathbf{y} = \pi R_0^2 = v_0.$$

For an isolated cell, the boundary is thus defined by $\{x \in \Omega, |x - x_i| = R_0\}$ and,

$$|\nabla_{\mathbf{y}}c(\mathbf{y}, \mathbf{x}_i)| = \frac{\alpha R_0^{\alpha-1}}{\lambda_{\alpha}} = \frac{\alpha(\alpha+2)}{2R_0}.$$

Consequently, the incompressibility force defined by Eq. (12) should scale like $|\nabla_{\mathbf{x}_i}\mathcal{T}_c(\hat{\mu})| \propto R_0$. We thus choose the gradient descent step in Eq. (11) to be normalized as $\tau \equiv \tau/R_0$ so that the gradient descent motion is independent of the size R_0 of the particles. Unless otherwise specified, we always use this normalization throughout the article.

Although the individual total cost of an isolated spherical particle does not depend on α , it will not be the case in crowded areas where particles need to adopt deformed shapes. Indeed, when $\alpha > 1$, the cost is a convex function of the distance between the point x and the centroid position x_i . Large deformations require the assignment of points \mathbf{y} far from the centroid position x_i and are thus strongly penalised. On the contrary, when $\alpha < 1$, the cost is a concave function of the distance, which allows larger deformations away from the rest ball shape. From this observation, the parameter α appears as a *hardness* parameter. In the three numerical experiments below, we confirm this interpretation by applying a constant force load to particles and measuring the deformation response for different values of α . Other quantitative and qualitative examples are presented in SM Appendix 2, in particular for a system of active Brownian particles and a model of crowd motion.

Remark 9 (Quotient method). *Another way of tuning the deformation properties of the particles is to consider the same cost for all the particles but different scaling factors λ_i in Eq. (6). This is similar to the so-called quotient method in [10]. An example is shown in the SM Video 2.*

3.2 Results

3.2.1 Falling soft spheres

We first apply a constant downward force to a small set of 30 particles, that is Eq. (14) with $N = 30$, $\sigma_i = 0$ and $\mathbf{b} = -F_0\vec{\mathbf{e}}_z$, where $\vec{\mathbf{e}}_z = (0, 1)^T$:

$$\dot{\mathbf{x}}_i = -F_0\vec{\mathbf{e}}_z - \tau\nabla_{\mathbf{x}_i}\mathcal{T}_c(\hat{\mu}).$$

In a crowded situation, illustrated in Fig. 7 and SM Videos 4,5,6, there is a competition between the repulsive incompressibility force and this gravity-like force. When α is small, the particles manage to squeeze their way by adopting elongated columnar shapes. When α increases, particles behave like hard-spheres and end up in a typical hexagonal packing situation.

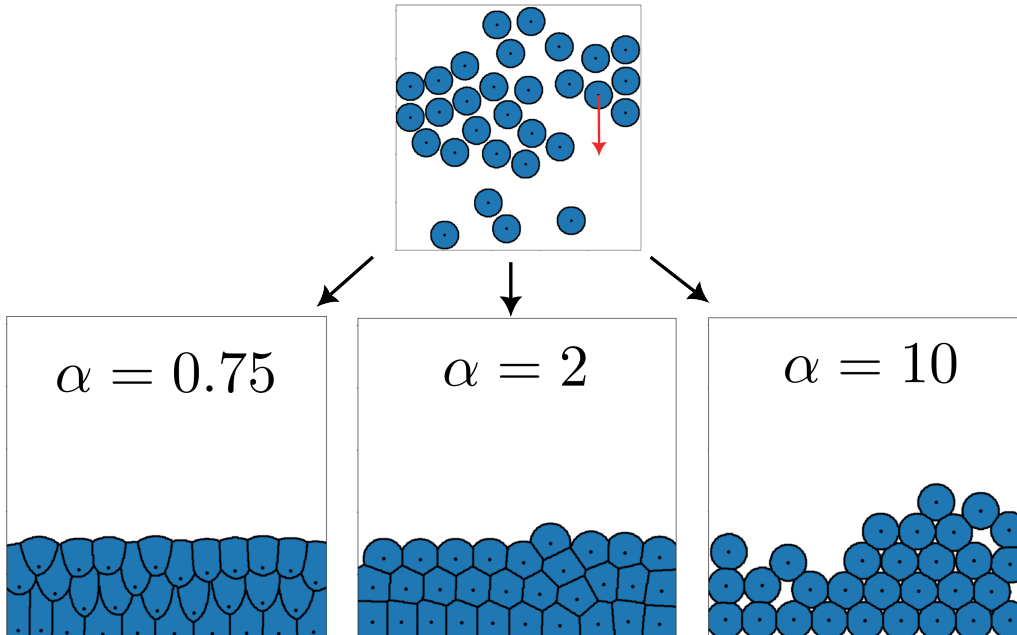


Figure 7: Initial configuration (top) and equilibrium configuration (bottom) of a system of falling soft spheres for three values of the deformation parameter α . For $\alpha = 0.75$, large deformations lead to more elongated and non-convex shapes (left). For $\alpha = 2$, the particles are convex and the equilibrium configuration is close to an hexagonal lattice (middle). For $\alpha = 10$, deformations from the base spherical shape are strongly penalized and the particles thus behave as hard-spheres (right). Parameters: grid size 512×512 , $\tau = 1.5$, $F_0 = 0.4$, $\Delta t = 0.001$. See also SM Videos 4,5,6.

3.2.2 Mixed spheres

Contrary to the cost function which encodes the deformability properties, the gradient step $\tau_i \equiv \tau_i/R_0$ in Eq. (14) represents the magnitude of the incompressibility force (relatively to the other forces) and may be interpreted as an inertia

parameter, typically the inverse of a mass. To illustrate this, we consider the same system of falling spheres but with half of the spheres being softer and various values of the parameter τ_i , which impact the final configuration. In Fig. 8 and SM Videos 7,8,9, we consider two types of particles, orange and blue, associated to two gradient steps, respectively τ_o and τ_b . Both types of particles obey the equation

$$\dot{\mathbf{x}}_i = -F_0 \vec{\mathbf{e}}_z - \tau_i \nabla_{\mathbf{x}_i} \mathcal{T}_c(\hat{\mu}),$$

with a constant force magnitude F_0 and $\tau_i = \tau_o$ when i is an orange particle and $\tau_i = \tau_b$ when i is a blue particle. Moreover, if the particle i is orange, it is associated to the cost $c(\mathbf{x}, \mathbf{x}_i) = \lambda_1^{-1} |\mathbf{x} - \mathbf{x}_i|$ and if it is blue, it is associated to the cost $c(\mathbf{x}, \mathbf{x}_i) = \lambda_2^{-1} |\mathbf{x} - \mathbf{x}_i|^2$. The orange particles are thus always softer than the blue particles but they are heavier when $\tau_o < \tau_b$ and lighter when $\tau_o > \tau_b$. As already observed in the previous experiments, due to the difference in the cost function, the soft orange particles tend to deform more than the hard blue particles. But specifically in this experiment, the effect of the gradient step value manifests through a sorting phenomenon which tends to push the lighter particles on top.

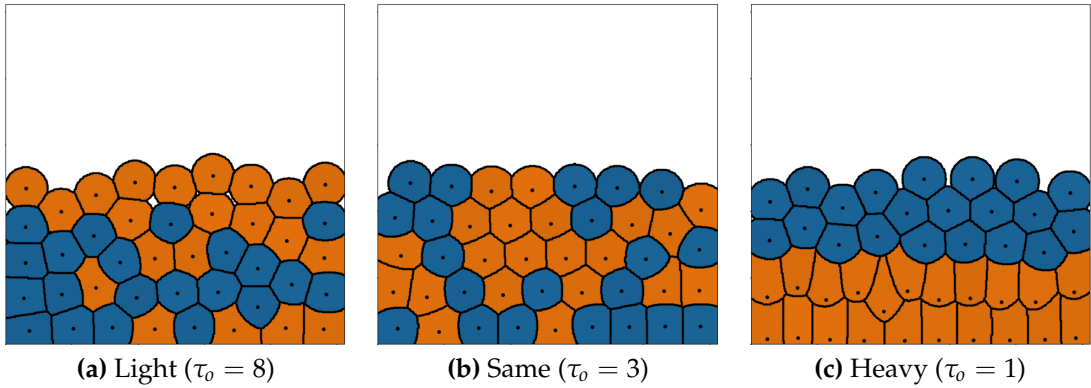


Figure 8: A mixed system of 30 falling spheres with 15 harder blue spheres ($\alpha = 2$) and 15 softer orange spheres ($\alpha = 1$). The gradient descent step of the blue spheres is fixed to $\tau_b = 3$ and both the orange and blue spheres are subject to the same downward force with magnitude $F_0 = 0.4$. The gradient descent step of the orange particles τ_o is analogous to the inverse of a mass. Consequently heavier orange particles tend to be lower. Parameters: grid size 512×512 , $\Delta t = 0.001$. See also SM Videos 7,8,9.

3.2.3 Micropipette aspiration

Viscoelastic properties of individual biological cells are often quantified using micropipette aspiration techniques [55, 51]: a single cell is first placed at the tip of a thin micropipette tube and a controlled pressure difference then creates an

aspiration force which sucks the cell inside the micropipette. The biomechanical properties are quantitatively evaluated by measuring the portion of the cell that effectively travels through the tube. This aspiration length ranges from zero for solid-like cell to the full tube for liquid-like cells. This experiment can be easily mimicked in silico by considering a micropipette-shaped domain Ω . Then, for a given set of fixed parameters (cell size, micropipette width, force magnitude τ_i), increasing the value of the deformability parameter α indeed lets us interpolate between liquid and solid particles. Tuning appropriately the cost function allows us to reproduce any visco-elastic cell, as illustrated in Fig. 9 and SM Video 10.

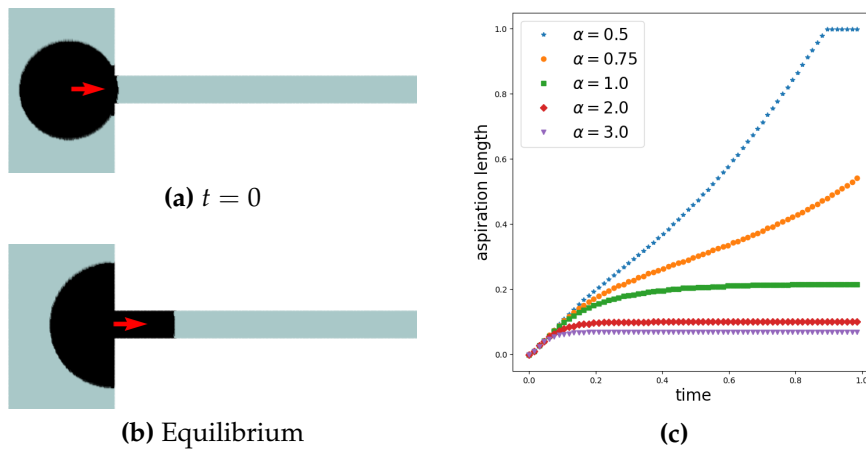


Figure 9: Micropipette experiment. (a)-(b) A single cell is sucked inside a thin tube by a constant force until it is blocked by the incompressibility force ($\alpha = 1$). (c) Aspiration length over time between 0 (outside the tube) and 1 (completely inside the tube) for different values of the deformability parameter α . See also SM Video 10.

4 Dynamical costs

In this section, we present two ways of making shapes evolve with time either by dynamically changing the parameters of the cost function or by applying local directional biases.

4.1 Orientation and alignment

The position x_i of a particle is often insufficient to describe the motion of active particles which also need to be endowed with an orientation. Typically, the orientation is a unit vector n_i which defines the direction of motion of the particle, as in flocking models. In cell biology, under the generic name of polarity, this vector may encode various structural differences which specify e.g. the migration direction, the division axis or some shape anisotropy. In this latter case, the

anisotropy can be further quantified by introducing an aspect ratio $a_i : b_i$ in dimension 2 or more generally a covariance matrix Σ_i in any dimension, which we always consider normalized to have determinant one in the following. We recall that in dimension 2, the matrix Σ_i is defined in terms of the polarity vector \mathbf{n}_i and the aspect ratio $s_i = a_i/b_i > 1$ by the eigenvector decomposition

$$\Sigma_i \mathbf{n}_i = \frac{a_i}{b_i} \mathbf{n}_i, \quad \Sigma_i \mathbf{n}_i^\perp = \frac{b_i}{a_i} \mathbf{n}_i^\perp,$$

where \mathbf{n}_i^\perp is the direct orthogonal vector to \mathbf{n}_i .

Oriented particles with anisotropic shapes can be realized in our optimal transport framework by considering appropriate cost functions which depend on s_i, \mathbf{n}_i or Σ_i . For instance, the following cost is a direct generalization of the isotropic L^2 cost Eq. (15) with scaling factor $\lambda > 0$,

$$c(\mathbf{x}, \mathbf{y}) = \lambda^{-1} (\mathbf{y} - \mathbf{x})^\top \Sigma^{-1} (\mathbf{y} - \mathbf{x}).$$

It corresponds to an ellipsoid shape with covariance matrix Σ . More refined shapes can be realized using cost functions of the form Eq. (8) with an appropriate function r_0 . A classical example in biology is the spherocylinder shape of 2D bacilli. Given a long axis vector $(\cos \theta_0, \sin \theta_0)^\top$ and an aspect ratio $s = a/b \geq 1$, this shape can be realized using the cost function associated to the function $r_0(\theta)$ defined by

$$r_0(\theta) = \begin{cases} \frac{b}{|\sin(\theta - \theta_0)|}, & \text{if } |\tan(\theta - \theta_0)| \geq \frac{1}{s-1}, \\ b \left(|\cos(\theta - \theta_0)| (s-1) + \sqrt{1 - ((s-1) \sin(\theta - \theta_0))^2} \right), & \text{otherwise.} \end{cases}$$

Coming back to a particle system, each particle is now endowed with its own cost function which may depend on the particle orientation vector \mathbf{n}_i , aspect ratio $s_i \geq 1$ or covariance matrix Σ_i . Just as the positions \mathbf{x}_i which evolve in time, there are several possible ways to model the evolution of these shape and orientation parameters. Since the pioneering work of Vicsek [143, 31, 144], in the literature on point particle systems, a popular class of models consider local alignment interactions by introducing a force typically of the form

$$\dot{\mathbf{n}}_i = \left(\text{Id} - \mathbf{n}_i \mathbf{n}_i^\top \right) \sum_{j \sim i} \mathbf{n}_j,$$

where the sum is over the indices j of the particles which are close to \mathbf{x}_i . This kind of interaction could of course be directly implemented in our model but it does not fully take into account the shapes of the particles. Actually, in polymer physics or in the modelling of swarms of rod-like bacteria, the local alignment observed experimentally is often understood as a consequence of collisions events

and volume exclusion effect between anisotropic shapes. In the Vicsek model and its numerous variants which focus on the consequences of alignment, it is then assumed as a model feature. Since our modelling framework can fully take into account the shape of the particles, we rather want to focus on the cause of alignment and confirm the idea that it emerges from the sole volume exclusion interactions and a natural assumption of local re-orientation due to collisions. A similar idea has recently been developed in [78, 72] in a computational model of deformable ellipsoidal particles representing fibroblasts.

In order to illustrate how to model changes of orientation due to volume exclusion in our framework, we simulate a simplistic model of bacterial swarm [35, 136] made of active spherocylindrical particles (Fig. 10 and SM Video 16). The equations of motion only contain a self-propulsion term and the incompressibility force which models volume exclusion:

$$\dot{\mathbf{x}}_i = c_0 \mathbf{n}_i - \tau \nabla_{\mathbf{x}_i} \mathcal{T}_c(\hat{\mu}),$$

where $c_0 > 0$ is the motion speed and $\mathbf{n}_i = (\cos \theta_i, \sin \theta_i)^\top$ is a unit vector in the direction given by the angle θ_i which defines the cost function $c(\mathbf{y}, \mathbf{x}_i)$ as above. The ‘‘collision’’ between two particles, which formally means that the associated Laguerre cells share a boundary, induces a shape change from the base shape which can be quantified by computing the empirical covariance matrix in the discrete setting:

$$\hat{\Sigma}_i = \frac{1}{N_i - 1} \sum_{\mathbf{y} \in \mathcal{L}_i} (\mathbf{y} - \mathbf{x}_i)(\mathbf{y} - \mathbf{x}_i)^\top, \quad N_i := \#\{\mathbf{y} \in \mathcal{L}_i\}.$$

We can therefore consider instantaneous plastic deformations, by defining the covariance of particle i at all time as

$$\Sigma_i = \frac{1}{\det(\hat{\Sigma}_i)^{1/d}} \hat{\Sigma}_i.$$

In dimension 2, this dynamics encodes at the same time the evolution of the polarity vector \mathbf{n}_i and the aspect ratio. In the numerical experiment below, particles represent bacteria with a fixed aspect ratio. Thus, only the direction of motion \mathbf{n}_i evolves, due to the bending effects of the collisions. Assuming that this directional change is much faster than the self-propelled motion, \mathbf{n}_i is defined at each time as the normalized eigenvector associated to the largest eigenvalue of the matrix $\hat{\Sigma}_i$ (with the sign correctly chosen to avoid flipping the direction of motion). Alternatively, one could also consider a nematic alignment process, for instance the relaxation equation

$$\dot{\mathbf{n}}_i = \frac{\nu}{2} \nabla_{\mathbf{n}_i} ((\mathbf{n}_i \cdot \hat{\mathbf{n}}_i)^2),$$

where $\hat{\mathbf{n}}_i$ is the normalized eigenvector associated to the largest eigenvalue of $\hat{\Sigma}_i$, ∇ denotes the spherical gradient and $\nu > 0$ is the relaxation rate. Both choices lead to long-range alignment and ordered motion shown in Fig. 10.

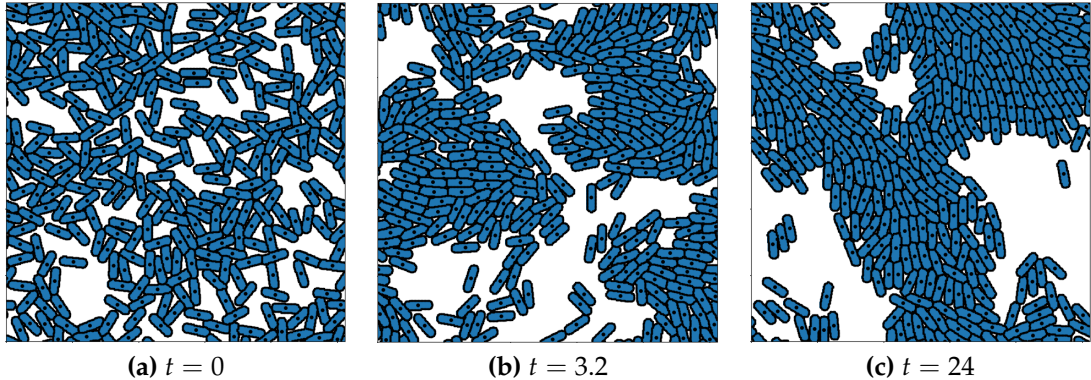


Figure 10: A swarm of rod-shaped particles with fixed aspect ratio 3 filling 65% of a periodic square domain. The direction of motion is defined at each time as the largest eigenvector of the empirical covariance matrix of the Laguerre cells. This collision process produces long-range alignment. Parameters: grid size 512×512 , $c_0 = 0.3$, $\tau = 0.25$, $\Delta t = 0.002$. See also SM Video 16.

4.2 Surface fluctuations

For some biological cells, the movement is induced by the deformation of their membrane, namely elongated protrusions, created randomly or in the direction of a stimulus, that the cell uses to pull itself forward. A fully realistic model of this complex process would require a detailed description of the cell internal structure (in particular its actin cortex) and its medium (the extra-cellular matrix as a fibrous viscoelastic material), like in [58, 148]. Taking into account all this complexity would certainly be challenging in our model and we do not claim that our model can achieve a comparable level of details. Aiming at a minimal phenomenological model, and recalling that the cell membrane can be modeled as the level set of the cost function, we model the local membrane deformations of a base spherical shape using a biased cost function. Since the cost is a nonnegative multiplicative quantity, we rather introduce the logarithmic potential

$$\varphi(\mathbf{x}, \mathbf{x}_i) = -\log c(\mathbf{x}, \mathbf{x}_i).$$

This potential φ will play a role similar to its homonym in the level-set method formalism [148]. In this classical setting [107, 106, 128], the dynamic on φ is given by PDE, for instance, like in [148], by

$$\partial_t \varphi(\mathbf{x}, \mathbf{x}_i) + \mathbf{v}(\mathbf{x}, \mathbf{x}_i) \cdot \nabla_{\mathbf{x}} \varphi(\mathbf{x}, \mathbf{x}_i) = 0,$$

where \mathbf{v} is a velocity field constructed by incorporating all the internal and external forces. Although theoretically possible in our setting, this approach poses technical difficulties linked to the implementation framework which requires an

analytical formula for the cost function (see SM Appendix 4). Such formula typically cannot be obtained by solving the above PDE. However, with a somehow simpler approach, we consider cost potentials of the form

$$\varphi = \varphi_0 + f,$$

where f is a (small) perturbation of the potential $\varphi_0 = -\log c_0$ associated to the base L^2 cost $c_0(\mathbf{x}, \mathbf{x}_i) = |\mathbf{x} - \mathbf{x}_i|^2 / R_0^2$ (for simplicity). This perturbation approach is similar to the model of deformable particles introduced in [104, 59, 118, 103] where f is constructed from a Fourier expansion with time-evolving coefficients. In our setting, the volume and non-overlapping constraints are automatically taken into account by the optimal transport solver and the incompressibility force, which gives more freedom on the choice of f . We will consider a perturbation f which models the shape deformations in the two following classical situations.

4.2.1 Chemotaxis movement

Many cells, like *Dictyostelium*, move in response to changes in the concentration of some chemical quantities in their medium. As explained in [148] and modeled using a level-set method, the movement is induced by morphological changes that we aim at reproduce. Similarly to [148], the level-set deformations are defined to match two known biological shapes.

We consider a chemo-attractant density $u(\mathbf{x})$ in Ω and we classically assume that a particle located at \mathbf{x}_i can sense the local gradient along the directions $\mathbf{x} - \mathbf{x}_i$, defined through the finite difference formula

$$\delta u(\mathbf{x}, \mathbf{x}_i) = \frac{u(\mathbf{x}) - u(\mathbf{x}_i)}{|\mathbf{x} - \mathbf{x}_i|}.$$

Then we introduce the biased cost potential

$$\varphi(\mathbf{x}, \mathbf{x}_i) = \varphi_0(\mathbf{x}, \mathbf{x}_i) + \beta f(\delta u(\mathbf{x}, \mathbf{x}_i)),$$

for some constant $\beta > 0$ and some function f which models how the gradient affects the deformation. Denoting by $\delta_+ = \max(0, \delta)$ the positive part of a number δ , a natural choice for f is

$$f(\delta) = -\delta_+, \tag{16}$$

which corresponds to lowering the potential and thus allowing deformations in the directions of large nonnegative gradients. This produces elongated shapes (see Fig 11 and SM Video 17). Another choice is to consider

$$f(\delta) = \delta_-^2 + \delta_+, \tag{17}$$

where $\delta_- = \max(0, -\delta)$ is the negative part of the number δ . This corresponds to a larger cost in the direction of larger gradient but even larger for negative gradient. This produces fan-like shapes (see Fig 11 and SM Video 18).

In both situations, we consider the simplest possible dynamics of the centroids

$$\dot{x}_i = -\tau \nabla_{x_i} \mathcal{T}_{c_0}(\hat{\mu}),$$

which, corresponds to movement in the direction of the barycenter (which is the gradient of the base L^2 cost, see Eq. (13)). Since the morphological changes are biased in the direction of increasing gradient, this choice induces chemotactic migration. An important point to note is that not only the volume is preserved regardless of the deformation, but this model also includes non-overlapping and cell-cell repulsion, thanks to the incompressibility force. As illustrated many times, crowded areas also induce other morphological changes which would typically be difficult to model in the level-set formalism (where mostly a single cell or non-interacting cells are considered).

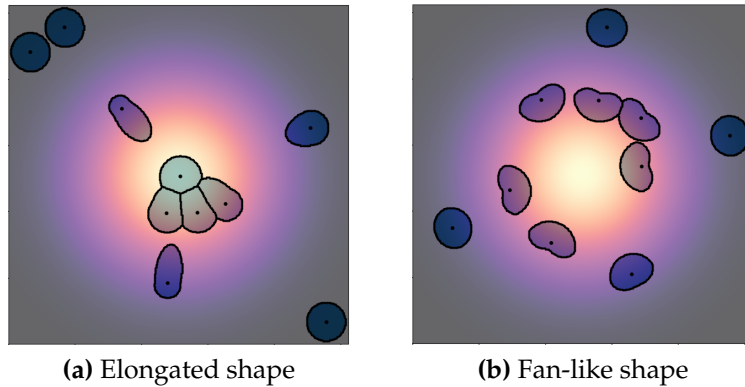


Figure 11: Chemotaxis motion induced by shape changes with two choices of perturbation functions. The chemo-attractant density is given by a Gaussian law with variance $\sigma = 0.2^2$ and is indicated by the underlying color field (a) Elongated shape obtained with Eq. (16). (b) Fan-like shape obtained with Eq. (17). Parameters: $\beta = 0.02$, $\tau = 1$, grid size 512×512 , $\Delta t = 0.01$. See also SM Videos 17,18.

4.2.2 Exploration via random protrusions

Mesenchymal cell migration is caused by a complex coordination between protrusion, adhesion and retraction [129]. Here we assume that cells evolve randomly without any external stimuli by following randomly created protrusions. We thus consider a cost perturbation of the form

$$f = - \sum_{k=1}^K \tilde{\zeta}_k G_{\theta_k}(\theta),$$

where K is the number of protrusions, θ_k are the polar angles defining their location in the membrane and $G_{\theta_k}(\theta)$ is the Gaussian density with center θ_k and a given variance which sets the width a protrusion. We assume that the elongation range (amplitude) of the protrusion ζ_k is constrained by $\zeta_k \geq 0$ and follows the stochastic differential equation

$$d\zeta_k = -\zeta_k dt + dB_t^k,$$

that is, protrusions are created randomly and naturally retract. To model the cytoskeleton of the cell, we also introduce an elastic force in the direction of the protrusions. The final equations of motion are thus given by:

$$\dot{\mathbf{x}}_i = \int_{\mathcal{L}_i} \frac{\mathbf{x} - \mathbf{x}_i}{|\mathbf{x} - \mathbf{x}_i|} \mathbb{1}_{|\mathbf{x} - \mathbf{x}_i| \geq R_0} d\mathbf{x} - \tau \nabla_{\mathbf{x}_i} \mathcal{T}_{c_0}(\hat{\mu}).$$

The result is presented in SM Video 19.

5 Surface interactions

In this section, we explain how to simulate interfacial forces and surface tension phenomena.

5.1 Goals and previous approaches

When several biological cells are in contact, or in contact with the medium, various interfacial forces lead to potential complex deformations and meaningful sorting phenomena. Such phenomena are of course of primary importance in developmental biology and various computational models have thus been proposed. The most archetypal results are obtained using cellular Potts, vertex or finite elements models which are particularly well-suited to describe the dynamics of tissues and dense aggregates. Due to their resemblance to soap bubbles, droplets and multi-phase systems, biological cell aggregates have often been modeled using the physics of capillarity and wetting phenomena in mind [36, 84, 95]. Over the last decades, the precise biological mechanisms and their implementation in mathematical models have been the subject of various debates, some of them are reviewed in [21, 105]. In a series of famous articles [32, 22, 23, 20], Chen and Brodland have proposed, and verified, the so-called Differential Interfacial Tension Hypothesis (DITH) which, in short, assumes that the various forces created by internal pressure, Cell Adhesion Molecules (CAM) etc, can all be resolved into a difference between equivalent surface tension parameters. This difference creates tangential forces at the interface between the cells (or the cells and the medium) which drive their local deformation and their spatial re-organisation.

In order to validate a computational model, the archetypal system considers an aggregate of two populations of cells immersed in a medium. Depending on the surface tension differences, Chen and Broadland have proposed a set of conditions which should lead to various sorting phenomena observed in biology, such as homophilic sorting, dissociation, engulfment, checkerboard patterning [3, 138]. The DITH can be implemented in various computational frameworks. In their work, Chen and Brodland have advocated the finite element method. Similarly to vertex models, in a finite element discretization the interfaces (edges) and junction points (vertices or nodes) are indeed handled directly as degrees of freedom. This represents a clear advantage to compute local force balances and interface deformation. However, it may come at the price of technical difficulties, in particular to deal with topological and connectivity changes, which are usually handled by-hand with ad hoc rules. Other powerful approaches which directly model the interface include the recent [94] which is based on a level-set method and a global energy minimization scheme of the contact surface. With a different perspective, point particle systems are intrinsically simpler, both theoretically and computationally, since mostly only binary attraction-repulsion forces between points are modeled. Unfortunately, with this somehow too simplified representation, it is typically impossible or difficult to reproduce the important sorting phenomena mentioned above [105]. More or less recent approaches, and in particular the so-called Self-Propelled Voronoi (SPV) and Active Vertex Models (AVM) [5, 9], are hybrid in the sense that they consider forces between the centers of a tessellation (thus treated as point particles) but the forces themselves are computed depending on the properties of a tessellation which is recomputed at each time step.

Our framework enters this latter hybrid approach where the positions x_i are the main degrees of freedom. In [5, 9], the authors consider Voronoi tessellation and they compute the forces applied to the cell centers as the negative gradient of some energy, typically built as a function of the cell perimeters. In comparison, we use a different tessellating procedure, which ensures a strict volume constraint but which makes the computation of such gradient much more difficult. Indeed, although theoretically implementable, computing the gradient of the interface lengths, or other related quantities, would require to compute the gradient of the Kantorovich potentials which appear in the definition of the Laguerre cells. Similar questions also appear in another context in [82] which introduces a meshing algorithm based on Laguerre tessellations. The differentiability properties of the solution of an optimal transport problem is a well-known but potentially involved question [38, 110] that we leave for future work. In the coming section, we follow a somehow simpler path, which is directly inspired by the physical approach of [20]. Instead of minimizing an energy, we compute pressure, surface tension and other interfacial forces that are applied directly to the centroids x_i . Naturally, the level of precision of our method cannot be compared to the one

of finite element models which can describe with an arbitrary precision the local deformations of a single cell [139] thanks to an arbitrary fine mesh. In comparison, in our framework, a particle is described by a single “macroscopic” mesh element. Nevertheless, for cell aggregates, where the cells are sufficiently small compared to the size of the system, we show that our method can accurately reproduce the complex sorting phenomena obtained with a finite element method in [20, 21], with a level-set method in [94], with a cellular Potts model in [53, 50, 7] and with a Voronoi tessellation method [134].

5.2 Forces

In our model, a particle is represented by a single Laguerre cell and should thus rather be considered as a macroscopic immersed body, where the surrounding environment is made of other cells or the medium. Following basic physical laws, we thus introduce a pressure-like force acting orthogonally to the boundary of each Laguerre cell and we assume that the resulting force acts on the centroid. More precisely, at the interface between two Laguerre cells, denoted by $\Gamma_{ij} = \mathcal{L}_i \cap \mathcal{L}_j$, (with possibly $j = 0$ in which case it is an interface between a particle and the medium), we define the following force which applies on x_i

$$\vec{F}_{j \rightarrow i} = -\frac{\gamma_{ij}}{|\mathbf{x}_j - \mathbf{x}_i|} \int_{\Gamma_{ij}} \vec{n} \, d\sigma, \quad \vec{F}_{0 \rightarrow i} = -\gamma_{i0} \int_{\Gamma_{i0}} \frac{\vec{n}}{|\sigma - \mathbf{x}_i|} \, d\sigma, \quad (18)$$

where \vec{n} is the outward normal to Γ_{ij} and $\gamma_{ij} > 0$ is an arbitrary coefficient. In dimension 3, γ_{ij} is a force per unit of length and can thus be directly understood as the surface tension between the particles i and j . In the 2D examples below, we keep this analogy and we also note that with this modelling choice, the equilibrium of a so-called cell doublet system is given by the Young-Dupré equation as it should be [86, 84, 95].

Lemma 10. *Let us consider two identical particles at positions \mathbf{x}_i and \mathbf{x}_j and the L^2 cost $c(\mathbf{x}, \mathbf{y}) = |\mathbf{y} - \mathbf{x}|^2$. We denote respectively by γ_{ij} and γ_0 the surface tensions between the particles i and j and between any of the particles and the medium. The equilibrium configuration, shown in Fig. 12, is made of two spherical caps with contact angle θ which satisfies*

$$\cos \theta = \frac{\gamma_{ij}}{2\gamma_0}.$$

Proof. The fact that the particles are spherical caps is a direct consequence of Theorem 3 (as Lemma 5). We denote by R their radius and θ the contact angle. The

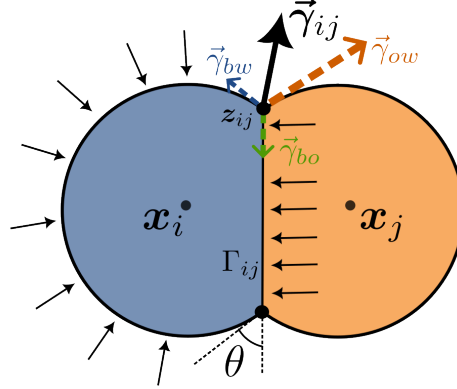


Figure 12: Geometry of a cell doublet

total force applied on x_i is thus equal to $\vec{F}_{j \rightarrow i} + \vec{F}_{0 \rightarrow i}$ with

$$\vec{F}_{j \rightarrow i} = -\frac{\gamma_{ij}}{|\mathbf{x}_j - \mathbf{x}_i|} \int_{\Gamma_{ij}} \vec{e}_{ij} d\sigma = -\gamma_{ij} \tan \theta \vec{e}_{ij},$$

$$\vec{F}_{0 \rightarrow i} = -\frac{\gamma_0}{R} \int_{\theta}^{2\pi - \theta} R(\cos \alpha \vec{e}_{ij} + \sin \alpha \vec{e}_{ij}^{\perp}) d\alpha = 2\gamma_0 \sin \theta \vec{e}_{ij}.$$

where $\vec{e}_{ij} = (\mathbf{x}_j - \mathbf{x}_i)/|\mathbf{x}_j - \mathbf{x}_i|$ and \vec{e}_{ij}^{\perp} is the direct orthogonal vector to \vec{e}_{ij} . The conclusion follows. \square

In [20, 23], the authors consider a force acting on each triple junction point z_{ijk} between three distinct particles i, j, k (with possibly $k = 0$), which is given by

$$\vec{\gamma}_{ijk} = \vec{\gamma}_{ij} + \vec{\gamma}_{jk} + \vec{\gamma}_{ki},$$

where $\vec{\gamma}_{ij}$ is the vector of magnitude $\gamma_{ij} > 0$ oriented outward along the boundary Γ_{ij} . In the cell-doublet system of Lemma 10, there are two triple junction points and $\vec{\gamma}_{ijk} = 0$ when the contact angle satisfies Young-Dupr e equation. As explained above, the triple junction points are computed automatically so we need to report these forces on the centroids. We simply assume a linear spring force between the centroids and the junction points, which can be interpreted as a very basic cytoskeleton model. This leads to the force

$$\vec{F}_{z_{ijk} \rightarrow i} = \left(\vec{\gamma}_{ij} \cdot \frac{\mathbf{z} - \mathbf{x}_i}{|\mathbf{z} - \mathbf{x}_i|} \right) \frac{\mathbf{z} - \mathbf{x}_i}{|\mathbf{z} - \mathbf{x}_i|}, \quad (19)$$

where \cdot denotes the Euclidean dot product.

5.3 Cell sorting experiments

We consider the dynamical system given by

$$\dot{\mathbf{x}}_i = \alpha \sum_{j=0}^N \vec{\mathbf{F}}_{j \rightarrow i} + \beta \sum_{j=1}^N \sum_{k=0}^N \vec{\mathbf{F}}_{z_{ijk} \rightarrow i} - \tau \nabla_{\mathbf{x}_i} \mathcal{T}(\hat{\mu}), \quad (20)$$

where the force in the first sum is equal to zero if the Laguerre cells i and j do not share a boundary and similarly in the second sum if the three Laguerre cells do not share a triple junction point. Moreover, although theoretically not necessary in this situation, the incompressibility force is added in the experiments below to ensure that the configuration remains sufficiently realistic and in particular that $\mathbf{x}_i \in \mathcal{L}_i$.

Following a classical experimental set up introduced in [22] and reviewed in [105, 21, 94], we consider an initial mixed aggregate with two types of cells (blue and orange) and we vary the five surface tension parameters, namely γ_b , γ_o , γ_{bo} , γ_{bw} and γ_{ow} , respectively between blue particles, orange particles, blue and orange particles, blue particles and the medium and orange particles and the medium. The simulation results are presented in Fig. 13 and SM Videos 20,21,22, where our model correctly captures the three following important configurations.

- Homophilic sorting with internalization of one of the population.
- Homophilic sorting with separation by the medium.
- Checkerboard patterning.

In addition, Fig. 14 and SM Video 23 show an engulfment phenomenon where the two populations are initially separated with a small contact interface before one population becomes internalized.

6 Discussion and conclusion

In this article we have introduced a novel approach to model, within a same framework, diverse biological systems ranging from individual deformable cells to complex tissue aggregates. The core idea is based on semi-discrete optimal transport theory and the notion of Laguerre tessellation, which together provide a natural way to represent arbitrary shapes and physical deformations with a strict volume constraint. We have verified the validity of our method by reproducing a wide range of classical models in computational biology. Although our method is formally an extension of the idea of Voronoi tessellation, we have highlighted formal links with other independent methods, in particular point-particle systems, level-set methods and vertex models. We also provide an efficient GPU implementation and a detailed documentation.

Since, to the best of our knowledge, our approach is new in the literature, the main focus of the present article was to validate it by comparison to other classical computational biology models, thus providing an independent validation

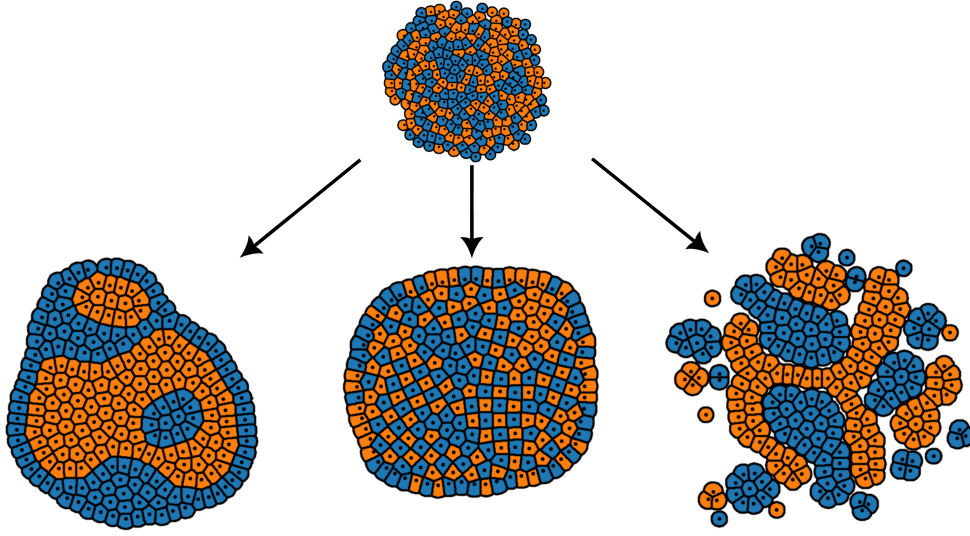


Figure 13: Sorting patterns in a mixture of two cell types, obtained from the same initial condition (top) under different conditions on the surface tensions. (Left) Internalization when $\gamma_{bo} < \gamma_{bw} - \gamma_{ow}$ ($\gamma_b = \gamma_o = 1, \gamma_{bo} = 5, \gamma_{ow} = 30, \gamma_{bw} = 7$). (Middle) Checkerboard when $\gamma_{bo} < \frac{1}{2}\gamma_b$ ($\gamma_b = \gamma_o = 7, \gamma_{bo} = 1, \gamma_{bw} = \gamma_{ow} = 30$). (Right) Separation when $\gamma_{bo} > \gamma_{bw} + \gamma_{ow}$ ($\gamma_b = \gamma_o = 1, \gamma_{bo} = 12, \gamma_{bw} = \gamma_{ow} = 5$). Parameters: $\tau = 0.5$, $\alpha = \beta = 0.14$, grid size 600×600 , $\Delta t = 0.0003$. See also SM Videos 20,21,22.

of their biological conclusions. The next important step is to seek a direct biological validation of our method by the confrontation to experimental data. In particular, our method seems well suited to the in silico modeling of the development of blastocysts. Recent experimental findings [64, 93] have identified several complex phenomena with morphological changes, sorting phenomena and dynamical topological properties via the formation of lumen. In order to understand the regulation processes between these phenomena, we need a mathematical model that can handle both individual cell deformations and their behaviors among dense aggregates. This seem particularly challenging using traditional methods, or at the price of an unreasonable computational cost, especially in a three-dimensional setting. This biological question was the initial motivation for the development of our method and is still an on-going work.

On the theoretical and numerical sides, several open questions and future improvements could be considered:

- Since our model has an intrinsic point-particle description, a natural question is to extend the active vertex theory developed in [5, 9, 134] to the case of Laguerre tessellations with volume constraint. This would lead to theoretical questions on the differentiability properties of the solution of an optimal transport problem.

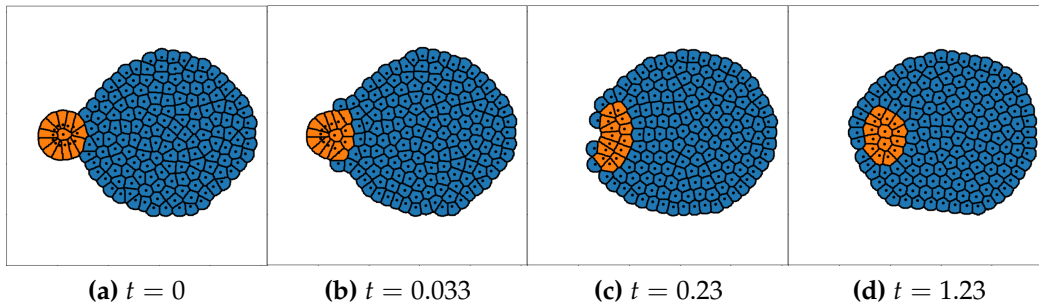


Figure 14: Engulfment of the orange cells inside the mass of blue cells. Parameters: $\tau = 0.5$, $\alpha = \beta = 0.14$, $\gamma_b = \gamma_o = 1$, $\gamma_{bo} = 5$, $\gamma_{ow} = 30$, $\gamma_{bw} = 7$, grid size 512×512 , $\Delta t = 0.0005$. See also SM Video 23.

- Another clear advantage of a point-particle description is the potential to derive coarse-grained PDE models that are better suited to mathematical analysis. For particles with a volume, this seems to be a largely open question, with the notable exception of [119, 100] in the context of crowd evacuation modeling. Our formal analysis (gathered in the SM Appendix 3) suggests a methodology based on mean-field theory that should lead to a novel general PDE modeling approach for soft-body systems.
- The theory of semi-discrete optimal transport theory is historically linked to the design of numerical schemes for fluid flows. Thus, it provides a direct way to include fluid-structure interactions between macroscopic cells immersed in a fluid environment. This corresponds to a more complex setting than the one considered in the present article, but which is typically considered in the so-called immersed boundary methods [109, 67, 116].
- Although our GPU implementation is general and quite efficient, several performance improvements could be considered for real-time large-scale simulations, especially in 3D. In particular, complex dynamical costs may be quite challenging to handle, especially when they are defined implicitly as the solution of a PDE as in level-set methods [148].

7 Supplementary Information

SM Appendix 1 (Section A). This section present the implementation details of the two benchmark experiments presented in the main text.

SM Appendix 2 (Section B). This section gathers additional numerical experiments which complement the conclusions in the main text and showcase other applications. We show how to handle motion in arbitrary domains, confirm an

important glass transition result for active Brownian particles and reproduce a crowd simulation leading to congestion effects.

SM Appendix 3 (Section C). This rather mathematical section formally explores the links between our agent-based model and coarse-grained PDE descriptions. We draw a parallel with related known results on crowd motion modeling and introduce a new general class of coupled Fokker-Planck-Monge-Ampère systems.

SM Appendix 4 (Section D). This section gathers reminders and classical results in measure theory and optimal transport.

The following supplementary videos can be found on Figshare at

<https://doi.org/10.6084/m9.figshare.25240669>

SM Video 1 (Incompressibility). Related to Fig. 3: simulation of a simple gradient descent dynamics in a four-cell system, where the negative gradient of the cost function (called incompressibility force) is displayed in red.

SM Video 2 (Run-and-tumble in a disk). Related to SM Appendix 2: simulation of a system of self-propelled particles with a constant speed motion, random direction changes and random energies in a disk domain.

SM Video 3 (Tissue growth). Related to SM Appendix 1: simulation of a basic tissue growth model in 2D based on division and cell growth starting from a single cell.

SM Video 4 (Falling spheres (1/6)). Related to Fig. 7: falling spheres with the deformation parameter $\alpha = 0.75$. Initially round shape cells adopt a columnar shape due to the external force and a high tolerance to deformation.

SM Video 5 (Falling spheres (2/6)). Related to Fig. 7: falling spheres with the deformation parameter $\alpha = 2$. The initially round particles are not so prone to deformation: they thus keep a convex shape and organize into a Voronoi-like configuration.

SM Video 6 (Falling spheres (3/6)). Related to Fig. 7: falling spheres with the deformation parameter $\alpha = 10$. The particles behave as hard-spheres.

SM Video 7 (Falling spheres (4/6)). Related to Fig. 8: falling spheres where the magnitude of the incompressibility force of the orange and blue spheres are respectively $\tau_o = 8$ and $\tau_b = 3$.

SM Video 8 (Falling spheres (5/6)). Related to Fig. 8: falling spheres where the magnitude of the incompressibility force of the orange and blue spheres are respectively $\tau_o = 3$ and $\tau_b = 3$.

SM Video 9 (Falling spheres (6/6)). Related to Fig. 8: falling spheres where the magnitude of the incompressibility force of the orange and blue spheres are respectively $\tau_o = 1$ and $\tau_b = 3$.

SM Video 10 (Micropipette aspiration). Related to Fig. 9: micropipette experiment for the deformability parameters $\alpha = 0.5, \alpha = 0.75, \alpha = 1, \alpha = 2$. The aspiration length decreases with the deformability.

SM Video 11 (Active Brownian Particles (1/3)). Related to SM Appendix 2: simulation of a system of active Brownian particles with deformability parameter $\alpha = 0.5$. The mean-square displacement of the particles is smaller but of the same order of magnitude than the theoretical value for independent point particles.

SM Video 12 (Active Brownian Particles (2/3)). Related to SM Appendix 2: simulation of a system of active Brownian particles with deformability parameter $\alpha = 2$. As the deformability decreases, the mean-square displacement is drastically reduced.

SM Video 13 (Active Brownian Particles (3/3)). Related to SM Appendix 2: simulation of a system of active Brownian particles with deformability parameter $\alpha = 10$. The particles behave as hard-spheres and self-organize into an optimal sphere packing configuration with almost no movement.

SM Video 14 (Crowd motion (1/2)). Related to SM Appendix 2: simulation of crowd motion towards a single exit point with deformability parameter $\alpha = 0.5$. All the particles manage to escape at the price of large deformations.

SM Video 15 (Crowd motion (2/2)). Related to SM Appendix 2: simulation of crowd motion towards a single exit point with deformability parameter $\alpha = 8$. The particles behave as hard-spheres and end up in a stable congested arch state.

SM Video 16 (Rod-shape particles). Related to Fig. 10: simulation of a system of rod-like particles with directional changes induced by deformation and bending effects. Long-range order spontaneously emerges after some time.

SM Video 17 (Chemotaxis motion (1/2)). Related to Fig. 11: simulation of a system of 10 particles where the movement is induced by the shape deformation in response to a chemo-attractant gradient. With a particular choice of cost perturbation, particles migrate by adopting elongated shapes in the direction of increasing chemo-attractant gradient.

SM Video 18 (Chemotaxis motion (2/2)). Related to Fig. 11: simulation of a system of 10 particles where the movement is induced by the shape deformation in response to a chemo-attractant gradient. With a particular choice of cost perturbation, particles migrate by adopting fan-like shapes orthogonal to the direction of increasing chemo-attractant gradient.

SM Video 19 (Random protrusions). Simulation of a random motion induced by random protrusions.

SM Video 20 (Cell sorting (1/3)). Related to Fig. 13: simulation of a two-population cell aggregate under the differential interfacial tension hypothesis. The orange cells are internalized inside the mass of blue cells.

SM Video 21 (Cell sorting (2/3)). Related to Fig. 13: simulation of a two-population cell aggregate under the differential interfacial tension hypothesis. The orange and blue cells self-organize into a checkerboard pattern state.

SM Video 22 (Cell sorting (3/3)). Related to Fig. 13: simulation of a two-population cell aggregate under the differential interfacial tension hypothesis. The orange and blue cells cluster with their own type and are separated by the medium.

SM Video 23 (Engulfment). Related to Fig. 14: simulation of a two-population cell aggregate under the differential interfacial tension hypothesis. The orange cells are initially completely outside the aggregate of blue cells but a small initial interface lead to the total engulfment of the orange cells inside the mass of blue cells.

SM Video 24 (Corner in 3D). 3D example where all the particles are attracted to a corner with a constant force. The blue particles are less deformable than the red particles. The video on the left-hand side shows the raw data computed on a grid of size $100 \times 100 \times 100$. In the video on the right-hand side the surface of each cell is smoothed: the support of each cell is first binarized and smoothed by a Gaussian of standard deviation equal to 1.5 pixel. The smooth surface is then defined as the level set of value 0.5.

SM Video 25 (Run-and-tumble in 3D). This is the same run-and-tumble system as in SM Video 2 but in a 3D cube. The darker particles are more deformable than the lighter ones. The smoothing procedure is the same as in SM Video 24.

SM Video 26 (3D hourglass). Falling soft spheres in a hourglass domain with a spherical obstacle. Particles are progressively added in the funnel. The color of a particle only indicates the time when it has been added. See also Fig. 4.

SM Video 27 (Benchmark: deformable ellipsoids). Benchmark experiment introduced in the main text for a system of $N = 1000$ self-propelled deformable ellipsoids with a discretization grid of size $M = 512$. See also Fig. 5 and Appendix 1 for the details of the model.

SM Video 28 (3D tissue growth). Growing cell aggregate in 3D following a basic somatic cell division process. See also Fig. 6 and SM 1.

Acknowledgments

This article was inspired by discussions with Takafumi Ichikawa on the modelling of embryonic development and with David Bourne, Maciej Buze and Steven Roper on the modelling of polycrystalline metals. The authors wish to thank Bruno Lévy, Roya Mohayaee, Steffen Plunder, Tsubasa Sukekawa, Tetsuya Hiraiwa and Sungrim Seirin-Lee for their insightful advice and for the useful discussions. The work of AD is supported by the following grant: KAKENHI Grant-in-Aid for Early-Career Scientists (Grant number 23K13015).

Supplementary material

A Details on the benchmarking experiments

For the benchmark experiment related to Table 1, the N self-propelled particles fill 80% of a bounded box, discretized on a grid of size M^3 . Each particle is endowed with the L^2 anisotropic cost

$$c(\mathbf{y}, \mathbf{x}_i) = \lambda_i^{-1} (\mathbf{y} - \mathbf{x}_i)^\top \Sigma_i^{-1} (\mathbf{y} - \mathbf{x}_i),$$

which models ellipsoid shapes. The orientation and aspect ratio of this base shape is updated at each time step following basic plastic deformation rules as explained in the 2D spherocylinder example (Fig. 10).

Specifically, at each time step, the direction of motion \mathbf{n}_i is defined as the maximal eigenvector of the empirical covariance matrix

$$\hat{\Sigma}_i = \frac{1}{N_i - 1} \sum_{\mathbf{y} \in \mathcal{L}_i} (\mathbf{y} - \mathbf{x}_i)(\mathbf{y} - \mathbf{x}_i)^\top, \quad N_i := \#\{\mathbf{y} \in \mathcal{L}_i\},$$

and the aspect ratio is defined as the ratio $\alpha_i = (\lambda_3 / \sqrt{\lambda_1 \lambda_2})^{2/3}$ where $\lambda_1 \leq \lambda_2 \leq \lambda_3$ are the eigenvalues of $\hat{\Sigma}_i$. The covariance matrix Σ_i is then computed as $\Sigma_i = RDR^\top$ where R is any rotation matrix the first column vector of which is \mathbf{n}_i and D is the diagonal matrix with entries $\alpha_i, \alpha_i^{-1/2}, \alpha_i^{-1/2}$.

In addition, we consider different volumes v_i randomly sampled with a ratio 1/5 between the smallest and the largest particles. The cost function is scaled so that the total cost of an isolated ellipsoid with small axis equal to 1 is equal to its volume times $C_i > 0$, where C_i is sampled between 3 and 4 independently for each particle.

In addition to the self-propulsion force with constant speed $c_0 = 0.3$, the only other force is the incompressibility force (11) with a gradient descent step $\tau_i = 42/R_i^2$ where $\frac{4}{3}\pi R_i^3 = v_i$ is the typical size of particle i .

For the benchmark experiment related to Fig. 6, we assume that the volume of the particles increases linearly

$$\dot{v}_i = \lambda_i \gamma$$

where λ_i is a uniform random variable between 0.5 and 2, independent for all the particles. The growth continues until the volume reaches the maximum v_{\max} . All the particles with a volume above 80% of v_{\max} divide in two along a random axis at a rate ν . In addition to the incompressibility force, all the particles are subject to an external cohesive force of magnitude F_0 oriented towards the center. The result in 2D is shown in Fig 15 and SM Video 3 on a constant box of size 512×512 . For the 3D case, we consider a constant resolution $400 \times 400 \times 400$ and progressively zoom out as the aggregate grows and until it reaches the size of a prescribed box appropriately scaled to fit $N = 50,000$ cells.

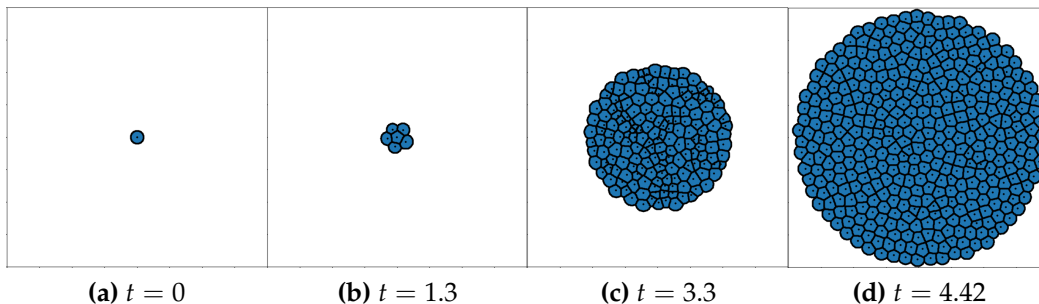


Figure 15: Growing tissue from 1 to 400 cells. Parameters: $\gamma = 1.8 \cdot 10^{-3}$, $\nu = 5$, $\tau = 1$, $F_0 = 0.2$, grid size 512×512 , $\Delta t = 0.01$. See also SM Video 3.

B Additional experiments

B.1 Run-and-tumble in a disk with energy differences

In this system, the particles are constrained to move inside a disk. They all have the same volume v_0 but unlike most of the other numerical experiments so far, the deformations are not handled by changing the cost function but rather by changing its scaling. We consider the L^2 cost

$$c(\mathbf{x}, \mathbf{x}_i) = \frac{2\lambda_i}{R_0^2} |\mathbf{x} - \mathbf{x}_i|^2,$$

where the scaling factor $\lambda_i > 0$ is sampled independently for each particles, so that

$$\int_{B(\mathbf{x}_i, R_0)} c(\mathbf{x}, \mathbf{x}_i) d\mathbf{x} = \lambda_i v_0.$$

Consequently, the boundary between two particles is always a circular arc as advocated in [10] under the name “quotient method”. However, particles associated to a lower λ_i have a smaller base cost and are thus prone to deformations.

The particle motion is given by a simple self-propelled motion

$$\dot{\mathbf{x}}_i = c_0 \mathbf{n}_i - \tau \nabla_{\mathbf{x}_i} \mathcal{T}_c(\hat{\mu}),$$

where $c_0 > 0$ and the direction \mathbf{n}_i is a unit vector which is re-sampled uniformly at rate ν (run-and-tumble). The result is shown in Fig. 16 and SM Video 2.

The same system in a three-dimensional setting is shown in SM Video 25.

B.2 Deformable active Brownian particles and glass transition

In [118, 9], a system of deformable active Brownian particles is considered and it is shown that when only little deformation is allowed (or when the self-propulsion

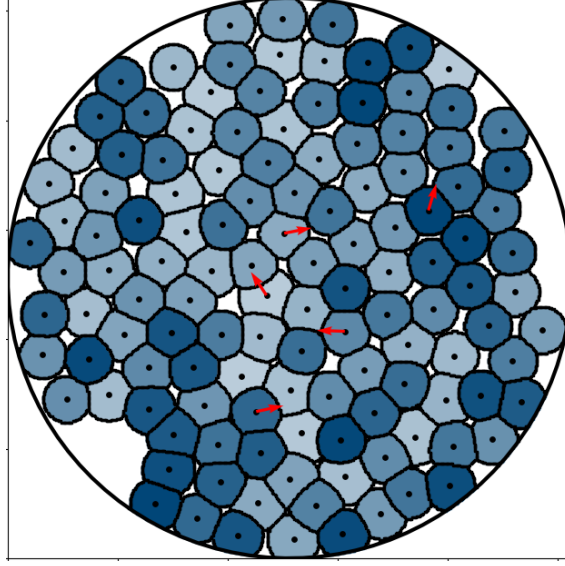


Figure 16: Particles filling 87.5% of a disk domain of radius 0.5 and different energies given by independent random variables λ_i sampled uniformly in the interval $(0.4, 3.5)$. Lighter color indicates lower energy (higher deformability). The red arrow indicates the direction of motion of a sample of five particles. Parameters: $c_0 = 0.4$, $\tau = 0.2$, $\nu = 1$, grid size 512×512 , $\Delta t = 0.0025$. See also SM Video 2.

force is too small), then the system end up in a solid state characterised by the optimal hexagonal packing of spherical particles. In our framework, the particle motion is given by the following system of equations:

$$\begin{aligned} dx_i &= c_0 n_i dt - \tau \nabla_{x_i} \mathcal{T}_c(\hat{\mu}) dt \\ dn_i &= (\text{Id} - n_i n_i^T) \circ \sqrt{2\sigma} dB_t^i, \end{aligned}$$

where n_i is a unit vector which defines the direction of motion and the B_t^i are independent two-dimensional Brownian motions. The projection operator $\text{Id} - n_i n_i^T$ ensures that $|n_i| = 1$ at all time (this corresponds to Brownian motion on the sphere) and this stochastic differential equation should be understood in the Stratonovich sense. As in the main text, in order to model deformability, the cost function is of the form

$$c(\mathbf{y}, \mathbf{x}) = \lambda_\alpha^{-1} |\mathbf{y} - \mathbf{x}|^\alpha,$$

with the same normalization constant λ_α as in the main text. The motion of the particles is measured by the Mean Square Displacement (MSD). For point particles, it is well known that the MSD grows linearly in time with a known theoretical rate. For soft spheres particles, the MSD seems to still grow linearly in time but with reduced rate (which seems to decrease geometrically with α). For $\alpha = 8$, the motion is almost impossible and we do observe a stable optimal sphere packing state as in [118]. See Fig 17 and SM Videos 11,12,13.

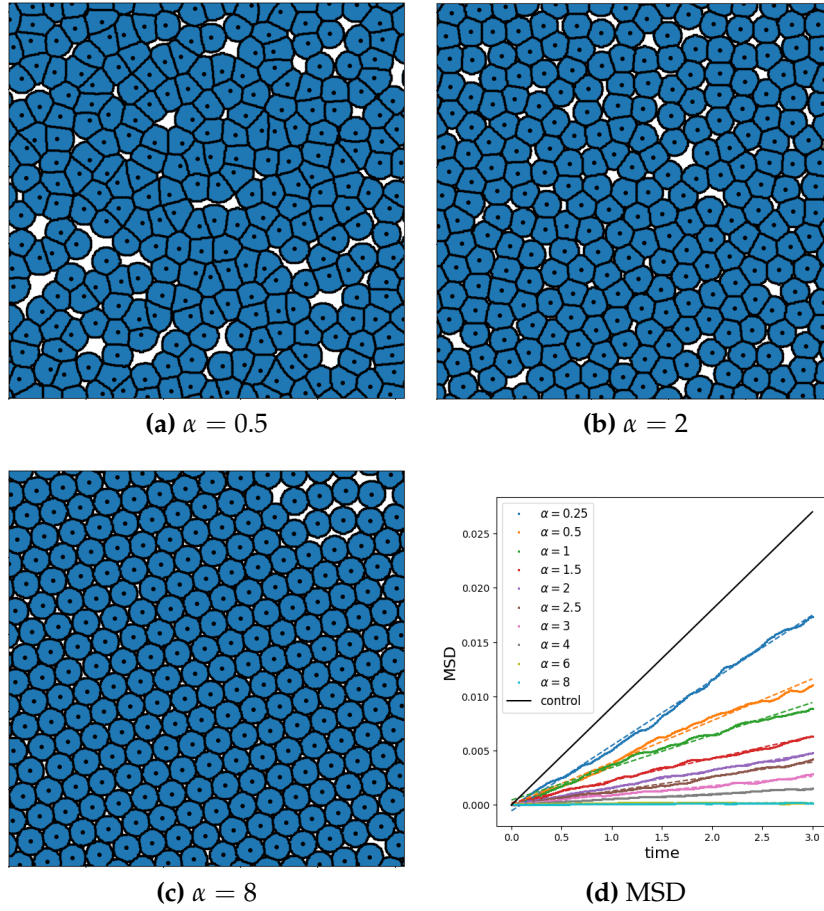


Figure 17: (a)-(c) Configuration at $t = 5$ of a system of 250 soft spheres filling 94% of a square periodic domain, for three values of the deformation parameter α . (d) Mean-square displacement as a function of α and linear fitting. Parameters: $c_0 = 0.3$, $\sigma = 20$, $\tau = 3$, grid size 512×512 , $\Delta t = 0.002$. See also SM Videos 11,12,13.

A natural question in this framework is to prove theoretically that the MSD grows linearly in time regardless of α (or not) and if it is the case, to compute the effective diffusion rate. For point particles, such computation can be carried out easily, for instance by studying the Fokker-Planck equation associated to the stochastic differential equation defining the motion of an active Brownian particle. In the present system, the non-overlapping interactions make this analysis much more difficult because there is no single Fokker-Planck equation describing the motion of a typical particle. Such equation could formally be obtained in the limit $N \rightarrow +\infty$ as discussed in SM Appendix 3. However, due to the nonlinear structure of this equation, the computation of the MSD is still an open question for us.

B.3 Crowd motion and congestion

In this numerical experiment, particles represent pedestrians in a crowd who all wish to escape a room via a single exit point. The motion is given by the same system of equations as in the case of falling spheres except that the force is directed towards the unique exit point. Some noise is also added to the direction of motion.

$$\begin{aligned} dx_i &= c_0 \mathbf{n}_i dt - \tau \nabla_{x_i} \mathcal{T}_c(\hat{\mu}) dt \\ dn_i &= (\text{Id} - \mathbf{n}_i \mathbf{n}_i^\top) \circ (\vec{\mathbf{b}}_0(x_i) dt + \sqrt{2\sigma} d\mathbf{B}_i^i), \end{aligned}$$

where $\vec{\mathbf{b}}_0(x_i)$ is a unit vector pointing towards the exit of the room and the cost belongs to the family of power costs as in the previous system of active Brownian particles. When the deformation parameter α is small, all the particles manage to exit the room at the price of strong deformations (SM Video 14). When α is too big, particles behave like hard-spheres and end up in a congested state, forming a stable arch around the exit point (Fig 18 and SM Videos 15).

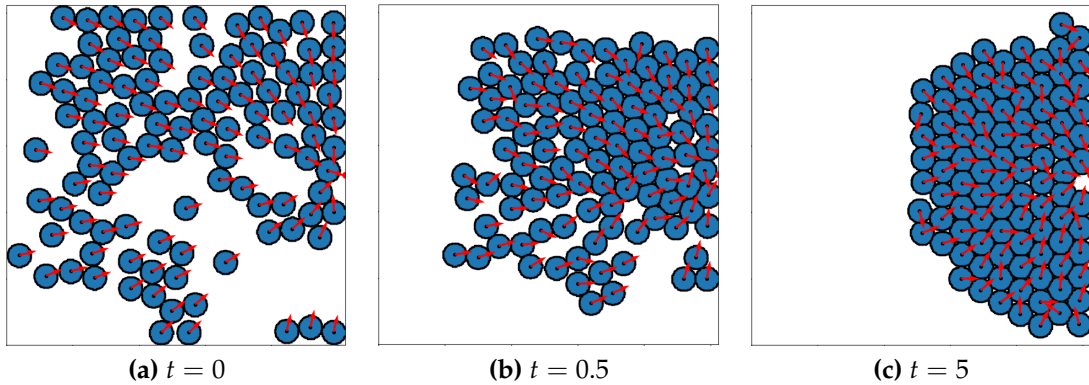


Figure 18: Simulation of an evacuation situation where each particle moves towards the exit (red dot at the center right part of the domain) up to some noise. There are initially 111 particles filling 42% of the room. The last arch configuration at $t = 5$ is stable and no particle manages to exit. Parameters: $\alpha = 8$, $c_0 = 0.4$, $\sigma = 0.2$, $\tau = 3$, grid size 512×512 , $\Delta t = 0.001$. See also SM Videos 15,14.

The mathematical modelling of crowd motion and congestion effect is notoriously difficult [85]. Usually, particles, representing pedestrians, are modelled by spheres with a tunable overlapping parameter. Our framework is slightly different as we rather consider physical deformations with a volume constraint (which may appear more natural). Both approaches seem to agree asymptotically in the sense that when no overlapping or no deformation is allowed, then the system is composed of hard-spheres and congestion effects such as stable arches appear. An important but difficult mathematical question is to model these phenomena

at the continuum PDE level, obtained as the scaling limit of an infinite number of particles. This question is discussed in SM Appendix 3 in relation to the previous works [85, 76, 120].

C Formal mean-field limit: the Fokker-Planck-Monge-Ampère system

There is a fundamental duality between agent-based and continuum PDE models in mathematical biology. Each description has its own strengths and weaknesses. Typically, agent-based models provide the finest level of details and modeling freedom and are naturally adapted to *in silico* computations with potentially stochastic components. However, they provide little room for theoretical mathematical analysis due to their complexity and usually high-dimensional nature. On the contrary, continuum PDE models provide a synoptic point of view at a statistical scale, benefit from all the analytical mathematical machinery, are often closer to physical laws and can eventually lead to much stronger “proved” conclusions. Bridging the gap between the two descriptions in a rigorous mathematical manner is a fundamental issue in mathematical biology but its feasibility strongly depends on the modeling framework [24]. Point-particle systems are classically the easier to coarse-grain, as they can often be written in a statistical physics framework for which many theoretical results are now available [28, 29]. Particles with a shape, regardless of the description (vertex models, cellular automata, phase-fields etc), seem much more difficult to handle, since no universal or natural continuum limit and scaling can be easily deduced. As such, the framework introduced in the present article can be seen as an intrinsically agent-based model. However formal computations (at this stage) and earlier works in computational optimal transport suggest that the underlying point-particle description can actually naturally lead to coarse-grained continuum models.

Let us recall the general form of the equations of motion of a particle system under the incompressibility force, external, possibly interacting, forces and independent Brownian noise:

$$dx_i = \mathbf{b}(x_i, \hat{\mu})dt - \tau \nabla_{x_i} \mathcal{T}_c(\hat{\mu})dt + \sqrt{2\sigma_i} dB_t^i. \quad (21)$$

Without the incompressibility force, this system is known as a McKean-Vlasov system and has been studied in great details since the seminal work of McKean [87] following the program introduced by Kac [69]. Review articles with a discussion of the numerous applications include [137, 97, 66, 28, 29]. The main idea, which originates from statistical physics, is to consider the limit of the sequence of random empirical measures $\hat{\mu} \equiv \hat{\mu}_N := \frac{1}{N} \sum_{i=1}^N \delta_{x_i}$ when $N \rightarrow +\infty$. When $\tau = 0$ and under some assumption on \mathbf{b} , it can be shown that this sequence has a

deterministic limit $\hat{\mu}_N \rightarrow f$ which is the solution of the (nonlinear) Fokker-Planck equation

$$\partial_t f = -\nabla_x \cdot (\mathbf{b}(x, f)f) + \Delta_x f.$$

This type of limit, called mean-field limit, is deeply linked to the notion of molecular chaos which originates from the work of Boltzmann and which has been formalised by Kac [69, 28, 29]. Within this framework, the solution f is the probability distribution of the state of a single typical particle and thus models the system at a statistical scale. Many important mathematical results, which are relevant in biology, have been obtained with this method, which could not all be cited here, see for instance [27] as an example for cell sorting and [29] for a review of other applications, in particular in collective dynamics.

Coming back to the Eq. (21), a first difficulty comes from the fact that the incompressibility force $\nabla_{x_i} \mathcal{T}_c(\hat{\mu})$ does not appear as a simple function of $\hat{\mu}$ due to the gradient in x_i . To overcome this issue, we recall the notion of first variation of a functional $\mathcal{F} : \mathcal{P}(\Omega) \rightarrow \mathbb{R}$ on the space of probability measure $\mathcal{P}(\Omega)$: this is the function $\frac{\delta \mathcal{F}}{\delta \mu}(\mu) : \Omega \rightarrow \mathbb{R}$ defined such that

$$\frac{d}{dh} \mathcal{F}(\mu + h\chi) \Big|_{h=0} = \int_{\Omega} \frac{\delta \mathcal{F}}{\delta \mu}(\mu) d\chi,$$

for every measure χ such that $\mu + h\chi \in \mathcal{P}(\Omega)$ for small enough h . With this notion, it is possible to apply the chain rule to compute the gradient

$$\nabla_{x_i} \mathcal{T}_c(\hat{\mu}) = N^{-1} \nabla \frac{\delta \mathcal{T}_c}{\delta \mu}(\hat{\mu})(x_i),$$

where the gradient on the right-hand side is the usual gradient of a real-valued function on \mathbb{R}^d . Thus taking the scale $\tau \equiv \tau_N = N\tau_0$, Eq. (21) can be rewritten,

$$dx_i = \mathbf{b}(x_i, \hat{\mu})dt - \tau_0 \nabla \frac{\delta \mathcal{T}_c}{\delta \mu}(\hat{\mu})(x_i)dt + \sqrt{2\sigma_i} d\mathbf{B}_t^i. \quad (22)$$

This latter equation enters the classical framework and lead to the formal mean-field limit

$$\partial_t f = -\nabla \cdot (\mathbf{b}(x, f)f) + \tau_0 \nabla \cdot \left(\nabla \frac{\delta \mathcal{T}_c}{\delta \mu}(f)f \right) + \Delta f. \quad (23)$$

At this stage, it remains to identify the first variation of the transport cost \mathcal{T}_c . We first note that if f satisfies Eq. (23), it should have a density with respect to the Lebesgue measure. We also assume that the cost is of the form $c(x, \mathbf{y}) = \ell(x - \mathbf{y})$ for a strictly convex function $\ell : \mathbb{R}^d \rightarrow [0, +\infty)$. Since the work of Brenier, McCann, Gbangbo, Cafferelli and others [17, 48, 26, 39], it is well-known that the Monge problem $T\#f = \text{Leb}$ has a unique solution which is of the form

$$T(x) = x - (\nabla \ell)^{-1}(\nabla \Phi(x)),$$

where Φ is a Kantorovich potential and it satisfies the Monge-Ampère equation [39]

$$|\det(\nabla T)| = f.$$

Then it can be shown [119, Proposition 7.17] that

$$\frac{\delta \mathcal{T}_c}{\delta \mu}(f) = \Phi.$$

Consequently, and after a few more computations [48], Eq. (23) can be rewritten as a coupled system of Fokker-Planck-Monge-Ampère equations

$$\partial_t f = -\nabla \cdot (\mathbf{b}(\mathbf{x}, f)f) + \tau_0 \nabla \cdot (\nabla \Phi f) + \Delta f. \quad (24a)$$

$$\det(\mathbf{I} - \nabla^2 \ell^*(\nabla \Phi) \nabla^2 \Phi) = f, \quad (24b)$$

where ℓ^* denotes the Legendre transform of ℓ defined by

$$\ell^*(\mathbf{y}) = \sup_{\mathbf{x} \in \mathbb{R}^d} \{\mathbf{x} \cdot \mathbf{y} - \ell(\mathbf{x})\}.$$

For the L^2 cost $c(\mathbf{x}, \mathbf{y}) = \frac{1}{2}|\mathbf{x} - \mathbf{y}|^2$, it holds that $\ell^* = \ell$ and thus $\nabla^2 \ell^*$ is the identity and Eq. (24b) reduces to

$$\det(\mathbf{I} - \nabla^2 \Phi) = f.$$

In this case, this system can also be derived less abstractly by using the direct expression, shown in [147],

$$\dot{\mathbf{x}}_i = -\tau \nabla_{\mathbf{x}_i} \mathcal{T}_c(\hat{\mu}) = \tau \int_{L_i} (\mathbf{x} - \mathbf{x}_i) d\mathbf{x} = \frac{\tau}{N} (\bar{\mathbf{x}}_i - \mathbf{x}_i) \quad (25)$$

where $\bar{\mathbf{x}}_i = N \int_{L_i} \mathbf{x} d\mathbf{x}$ is the barycenter of the Laguerre cell. In this semi-discrete setting, there is no Monge map sending $\hat{\mu}$ to the Lebesgue measure. However, it is natural to think that as $N \rightarrow +\infty$, the Laguerre cells shrinks to a single point and if $\hat{\mu} \rightarrow f$, then the barycentric map $\mathbf{x}_i \mapsto \bar{\mathbf{x}}_i$ should behave like the map T which sends the continuous measure f to the Lebesgue measure.

Actually, a particle system similar to Eq. (25) has been studied in [76] with the important difference that the Laguerre cell is associated to the more involved semi-discrete optimal transport problem where the Lebesgue measure is replaced by the projection of $\hat{\mu}$ on the set of probability density functions ρ which satisfies $\rho \leq 1$. In this case, the limit $\hat{\mu} \rightarrow \rho$ is proved (for a particular scaling) where ρ is a weak solution of the system

$$\begin{aligned} \partial_t \rho + \nabla \cdot (\rho v) &= 0, \\ v &= -\nabla p, \\ p &\geq 0, p(1 - \rho) = 0. \end{aligned}$$

This latter system is introduced as a model of crowd motion with the congestion constraint $\rho \leq 1$. We also refer to [120] and to [85] for an in-depth discussion of this subject. See also [100] for a similar approach leading to porous media equations. Note also that in these works, the particle system is not introduced per se but rather as a particle discretization scheme of a PDE model, following the fruitful gradient flow theory developed by Otto, Jordan and Kinderlehrer [119, Chapter 8]

Our approach is somehow simpler, as we only consider the Lebesgue measure as the source measure of the semi-discrete optimal transport model. However, our starting point is the particle system and for arbitrary costs, the more abstract formulation Eqs. (22)-(24) seems more appropriate. In the numerical experiments on crowd motion in SM Appendix 2, the typical congestion effect, materialized by the formation of stable arches, seems to also appear by taking the hard-sphere limit ($\alpha \rightarrow +\infty$) starting from deformable soft spheres. It would be interesting to study if such limit can be derived in the Fokker-Planck-Monge-Ampère system Eq. (24). This system is not so common in literature, with the exception of [15] where a special case is studied in connection with the Euler equations. This idea thus seems to open many interesting, rather theoretical questions, in particular regarding the following topics.

- The rigorous mean-field limit $\hat{\mu} \rightarrow f$, in the presence of stochastic terms: to the best of our knowledge, it seems to be an open question, although it may be linked to optimal control systems (see [120]).
- Are there other scaling limits, in particular when the cost depends on N , as in the finite energy scaling discussed in the main text? Related questions for the solutions of Eq. (24) are also interesting: in particular when $\nabla\Phi = o(1)$ in which case the Monge-Ampère equation reduces to a simpler elliptic equation and the full system Eq. (24) to a parabolic-elliptic system which can be seen as a Keller-Segel system with dispersion instead of concentration.
- What happens for more complex transport costs? In particular, in the numerical experiments, the transport cost is rather of the form

$$\hat{\mu}, \hat{\mu}_0 \mapsto \mathcal{T}_c(V\hat{\mu} + (1 - V)\hat{\mu}_0),$$

where $V < 1$ is the volume occupied by the particle and $\hat{\mu}_0$ is a discretization of the free space (either with one particle with zero cost or many small particles).

D Optimal transport reminders

We gather here some important definitions and results that may be useful for a better understanding of the main text. Optimal transport theory is by now well-established and we refer to the classical references [119, 145, 146] for a deeper introduction to the subject from a mathematical perspective and to [110, 43] for a focus on numerical methods and applications in data sciences and computational geometry.

Historically, Monge considered the problem of transporting sand piles located at some positions $\mathbf{y}_1, \dots, \mathbf{y}_M \in \Omega \subset \mathbb{R}^d$ and with respective masses β_1, \dots, β_M , to some target positions $\mathbf{x}_1, \dots, \mathbf{x}_N \in \Omega$ that should respectively receive a volume $\alpha_1, \dots, \alpha_N$ of sand. The total volume $\sum_j \beta_j = \sum_i \alpha_i = 1$ is classically normalized to 1. The transport of a sand grain between the locations \mathbf{y} and \mathbf{x} comes with a cost $c(\mathbf{y}, \mathbf{x})$; the optimal transport problem is to find an optimal way of moving all of the sand at a minimal cost. When $N = M$ and $\alpha_i = \beta_j = 1/N$, this problem can be seen as a *matching* problem, which consists in finding the one-to-one map (or equivalently a permutation of the set $\{1, \dots, N\}$)

$$T : \{\mathbf{y}_1, \dots, \mathbf{y}_N\} \rightarrow \{\mathbf{x}_1, \dots, \mathbf{x}_N\},$$

that minimizes the total transport cost

$$\mathcal{T}_c := \frac{1}{N} \sum_{i=1}^N c(\mathbf{y}_i, T(\mathbf{y}_i)).$$

In the general case with $N \neq M$ and arbitrary volumes, such a *Monge map* may not exist since we may have to split the sand piles and send their different parts to different locations. The optimal transport problem then only makes sense for the more general notion of *transport plan* introduced by Kantorovich. In this setting, a transport plan is a $N \times M$ matrix $\pi = (\pi_{ij})$ whose non-negative coefficients $\pi_{ij} \geq 0$ indicate how much of the sand pile j is sent to the location i . Consequently, the transport plan π should satisfy the constraints

$$\forall j, \sum_{i=1}^N \pi_{ij} = \beta_j, \quad \forall i, \sum_{j=1}^M \pi_{ij} = \alpha_i.$$

The optimal transport problem then consists in finding the matrix π that satisfies this constraints and minimizes the total transport cost

$$\mathcal{T}_c := \sum_{i=1}^N \sum_{j=1}^M \pi_{ij} c(\mathbf{y}_j, \mathbf{x}_i).$$

Going further, this problem can be generalized further to both continuous and discrete probability measures. The sand piles and target locations are respectively

modeled by the discrete probability measures

$$v = \sum_{j=1}^M \beta_j \delta_{y_j}, \quad \mu = \sum_{i=1}^N \alpha_i \delta_{x_i}. \quad (26)$$

The Monge problem corresponds to the minimization problem

$$\inf_{T: \Omega \rightarrow \Omega} \left\{ \int_{\Omega} c(\mathbf{y}, T(\mathbf{y})) v(d\mathbf{y}) \mid T\#v = \mu \right\}, \quad (27)$$

where we recall that the *push-forward* measure $T\#v$ is defined as the measure on Ω such that

$$T\#v(\mathcal{B}) = v(T^{-1}(\mathcal{B})),$$

for all open sets \mathcal{B} .

The Kantorovich problem corresponds to the minimization problem

$$\inf_{\Pi \in \mathcal{P}(\Omega \times \Omega)} \left\{ \int_{\Omega} \int_{\Omega} c(\mathbf{y}, \mathbf{x}) \Pi(d\mathbf{y}, d\mathbf{x}) \mid \Pi_1 = v, \Pi_2 = \mu \right\}, \quad (28)$$

where $\mathcal{P}(\Omega \times \Omega)$ denotes the set of probability measures on $\Omega \times \Omega$ and Π_1 and Π_2 are the first and second marginals of $\Pi \in \mathcal{P}(\Omega \times \Omega)$.

Although it can be checked that with the choice Eq. (26), the Monge and Kantorovich problems reduce to the optimization problems introduced above, the formulations Eqs. (27)-(28) are much more general and are not restricted to the case of discrete measures μ, v . In particular, μ and/or v can be continuous measures (i.e. defined by a probability density function), in which case the following fundamental theorem due to Brenier, Gangbo, McCann, Caffarelli and others [17, 48, 26] can be proved.

Theorem 11. *If the source measure v is a continuous measure and under some assumptions on the cost function c , then the Monge problem Eq. (27) has a unique solution T .*

In our approach, we consider the semi-discrete case where v is a continuous measure and $\mu = \sum_i \alpha_i \delta_{x_i}$ is a discrete measure. In this case, a direct application of the previous theorem shows that the optimal transport problem is equivalent to the computation of a partition of the space $\Omega = \cup_i \mathcal{S}_i$ into the disjoint sets:

$$\mathcal{S}_i := T^{-1}(\{x_i\}).$$

Moreover, a simple computation, presented in the main text in the special case where v is the Lebesgue measure, shows that $v(\mathcal{S}_i) = \alpha_i$. A graphical illustration of the discrete, continuous and semi-discrete problems is shown in Fig. 19.

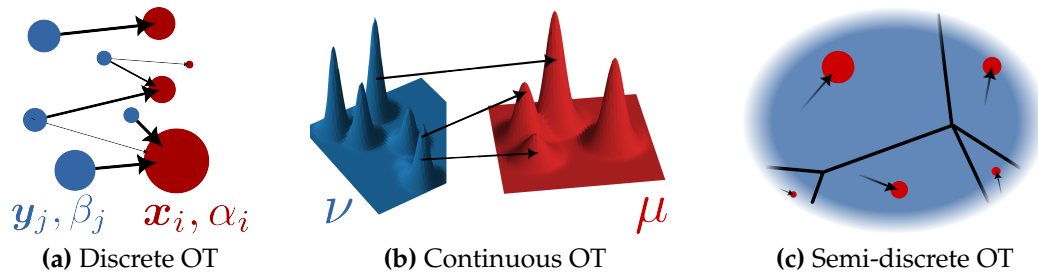


Figure 19: Discrete, continuous and semi-discrete optimal transport. (a) A discrete optimal transport problem is a matching point problem but which may require mass splitting in which case there is no Monge map. (b) If the source measure has a density, then there is a Monge map. (c) In the semi-discrete case, the target measure is discrete and the Monge map defines a partition of the space.

References

- [1] A. Alpers, A. Brieden, P. Gritzmann, A. Lyckegaard, and H. F. Poulsen. “Generalized Balanced Power Diagrams for 3D Representations of Polycrystals”. *Philosophical Magazine* 95.9 (2015), pp. 1016–1028. DOI: 10.1080/14786435.2015.1015469.
- [2] S. Alt, P. Ganguly, and G. Salbreux. “Vertex Models: From Cell Mechanics to Tissue Morphogenesis”. *Phil. Trans. R. Soc. B* 372.1720 (2017), p. 20150520. DOI: 10.1098/rstb.2015.0520.
- [3] P. B. Armstrong. “Cell Sorting Out: The Self-Assembly of Tissues *In Vitro*”. *Critical Reviews in Biochemistry and Molecular Biology* 24.2 (1989), pp. 119–149. DOI: 10.3109/10409238909086396.
- [4] U. Ayachit. *The Paraview Guide: A Parallel Visualization Application*. Kitware, Inc., 2015.
- [5] D. L. Barton, S. Henkes, C. J. Weijer, and R. Sknepnek. “Active Vertex Model for Cell-Resolution Description of Epithelial Tissue Mechanics”. *PLoS Comput. Biol.* 13.6 (2017). Ed. by S. Shvartsman, e1005569. DOI: 10.1371/journal.pcbi.1005569.
- [6] C. Bechinger, R. Di Leonardo, H. Löwen, C. Reichhardt, G. Volpe, and G. Volpe. “Active Particles in Complex and Crowded Environments”. *Rev. Mod. Phys.* 88.4 (2016), p. 045006. DOI: 10.1103/RevModPhys.88.045006.
- [7] R. Belousov, S. Savino, P. Moghe, T. Hiiragi, L. Rondoni, and A. Erzberger. “When Time Matters: Poissonian Cellular Potts Models Reveal Nonequilibrium Kinetics of Cell Sorting”. 2023. arXiv: 2306.04443.

- [8] D. Bi, J. H. Lopez, J. M. Schwarz, and M. L. Manning. “A Density-Independent Rigidity Transition in Biological Tissues”. *Nature Physics* 11.12 (2015), pp. 1074–1079. DOI: 10.1038/nphys3471.
- [9] D. Bi, X. Yang, M. C. Marchetti, and M. L. Manning. “Motility-Driven Glass and Jamming Transitions in Biological Tissues”. *Physical Review X* 6.2 (2016), p. 021011. DOI: 10.1103/PhysRevX.6.021011.
- [10] M. Bock, A. K. Tyagi, J.-U. Kreft, and W. Alt. “Generalized Voronoi Tessellation as a Model of Two-dimensional Cell Tissue Dynamics”. *Bull. Math. Biol.* 72.7 (2010), pp. 1696–1731. DOI: 10.1007/s11538-009-9498-3.
- [11] D. P. Bourne, P. J. J. Kok, S. M. Roper, and W. D. T. Spanjer. “Laguerre Tessellations and Polycrystalline Microstructures: A Fast Algorithm for Generating Grains of given Volumes”. *Philosophical Magazine* 100.21 (2020), pp. 2677–2707. DOI: 10.1080/14786435.2020.1790053.
- [12] D. P. Bourne. *MATLAB-SDOT*. GitHub repository. URL: <https://github.com/DPBourne/MATLAB-SDOT>.
- [13] D. P. Bourne, B. Schmitzer, and B. Wirth. “Semi-Discrete Unbalanced Optimal Transport and Quantization”. 2018. arXiv: 1808.01962.
- [14] D. Bourne, M. Pearce, and S. Roper. “Geometric Modelling of Polycrystalline Materials: Laguerre Tessellations and Periodic Semi-Discrete Optimal Transport”. *Mechanics Research Communications* 127 (2023), p. 104023. DOI: 10.1016/j.mechrescom.2022.104023.
- [15] Y. Brenier and G. Loeper. “A Geometric Approximation to the Euler Equations: The Vlasov-Monge-Ampère System”. *GAFSA, Geom. funct. anal.* 14.6 (2004), pp. 1182–1218. DOI: 10.1007/s00039-004-0488-1.
- [16] Y. Brenier. “A Combinatorial Algorithm for the Euler Equations of Incompressible Flows”. *Computer Methods in Applied Mechanics and Engineering* 75.1-3 (1989), pp. 325–332. DOI: 10.1016/0045-7825(89)90033-9.
- [17] Y. Brenier. “Polar Factorization and Monotone Rearrangement of Vector-valued Functions”. *Comm. Pure Appl. Math.* 44.4 (1991), pp. 375–417. DOI: 10.1002/cpa.3160440402.
- [18] Y. Brenier. “Derivation of the Euler Equations from a Caricature of Coulomb Interaction”. *Comm. Math. Phys.* 212.1 (2000), pp. 93–104. DOI: 10.1007/s002200000204.
- [19] Y. Brenier. “Optimal Transportation of Particles, Fluids and Currents”. In: *Variational Methods for Evolving Objects*. Hokkaido University, Sapporo, Japan, 2015, pp. 59–85. DOI: 10.2969/aspm/06710059.

- [20] G. W. Brodland. “The Differential Interfacial Tension Hypothesis (DITH): A Comprehensive Theory for the Self-Rearrangement of Embryonic Cells and Tissues”. *Journal of Biomechanical Engineering* 124.2 (2002), pp. 188–197. DOI: 10.1115/1.1449491.
- [21] G. W. Brodland. “Computational Modeling of Cell Sorting, Tissue Engulfment, and Related Phenomena: A Review”. *Applied Mechanics Reviews* 57.1 (2004), pp. 47–76. DOI: 10.1115/1.1583758.
- [22] G. W. Brodland and H. H. Chen. “The Mechanics of Cell Sorting and Envelopment”. *Journal of Biomechanics* 33.7 (2000), pp. 845–851. DOI: 10.1016/S0021-9290(00)00011-7.
- [23] G. W. Brodland and H. H. Chen. “The Mechanics of Heterotypic Cell Aggregates: Insights From Computer Simulations”. *Journal of Biomechanical Engineering* 122.4 (2000), pp. 402–407. DOI: 10.1115/1.1288205.
- [24] A. Buttenschön and L. Edelstein-Keshet. “Bridging from Single to Collective Cell Migration: A Review of Models and Links to Experiments”. *PLoS Comput. Biol.* 16.12 (2020). Ed. by A. Mogilner, e1008411. DOI: 10.1371/journal.pcbi.1008411.
- [25] M. Buze, J. Feydy, S. M. Roper, K. Sedighiani, and D. P. Bourne. “Anisotropic Power Diagrams for Polycrystal Modelling: Efficient Generation of Curved Grains via Optimal Transport”. 2024. arXiv: 2403.03571. URL: <http://arxiv.org/abs/2403.03571>.
- [26] L. Caffarelli. “Allocation Maps with General Cost Functions”. In: *Partial Differential Equations and Applications. Collected Papers in Honor of Carlo Pucci*. Ed. by G. Talenti. CRC Press, 1996.
- [27] J. A. Carrillo, H. Murakawa, M. Sato, H. Togashi, and O. Trush. “A Population Dynamics Model of Cell-Cell Adhesion Incorporating Population Pressure and Density Saturation”. *J. Theoret. Biol.* 474 (2019), pp. 14–24. DOI: 10.1016/j.jtbi.2019.04.023.
- [28] L.-P. Chaintron and A. Diez. “Propagation of Chaos: A Review of Models, Methods and Applications. I. Models and Methods”. *Kinet. Relat. Models* 15.6 (2022), pp. 895–1015. DOI: 10.3934/krm.2022017.
- [29] L.-P. Chaintron and A. Diez. “Propagation of Chaos: A Review of Models, Methods and Applications. II. Applications”. *Kinet. Relat. Models* 15.6 (2022), pp. 1017–1173. DOI: 10.3934/krm.2022018.
- [30] B. Charlier, J. Feydy, J. A. Glaunès, F.-D. Collin, and G. Durif. “Kernel Operations on the GPU, with Autodiff, without Memory Overflows”. *J. Mach. Learn. Res.* 22.74 (2021), pp. 1–6.

- [31] H. Chaté, F. Ginelli, G. Grégoire, and F. Raynaud. “Collective Motion of Self-Propelled Particles Interacting without Cohesion”. *Phys. Rev. E* 77.4 (2008), p. 046113. DOI: 10.1103/PhysRevE.77.046113.
- [32] H. H. Chen and G. W. Brodland. “Cell-Level Finite Element Studies of Viscous Cells in Planar Aggregates”. *Journal of Biomechanical Engineering* 122.4 (2000), pp. 394–401. DOI: 10.1115/1.1286563.
- [33] R. Cohen, L. Amir-Zilberstein, M. Hersch, S. Woland, O. Loza, S. Taiber, F. Matsuzaki, S. Bergmann, K. B. Avraham, and D. Sprinzak. “Mechanical Forces Drive Ordered Patterning of Hair Cells in the Mammalian Inner Ear”. *Nat. Commun.* 11.1 (2020), p. 5137. DOI: 10.1038/s41467-020-18894-8.
- [34] F. Cooper, R. Baker, M. Bernabeu, R. Bordas, L. Bowler, A. Bueno-Orovio, H. Byrne, V. Carapella, L. Cardone-Noott, J. Cooper, S. Dutta, B. Evans, A. Fletcher, J. Grogan, W. Guo, D. Harvey, M. Hendrix, D. Kay, J. Kursawe, P. Maini, B. McMillan, G. Mirams, J. Osborne, P. Pathmanathan, J. Pitt-Francis, M. Robinson, B. Rodriguez, R. Spiteri, and D. Gavaghan. “Chaste: Cancer, Heart and Soft Tissue Environment”. *Journal of Open Source Software* 5.47 (2020), p. 1848. DOI: 10.21105/joss.01848.
- [35] N. C. Darnton, L. Turner, S. Rojevsky, and H. C. Berg. “Dynamics of Bacterial Swarming”. *Biophysical Journal* 98.10 (2010), pp. 2082–2090. DOI: 10.1016/j.bpj.2010.01.053.
- [36] P.-G. De Gennes, F. Brochard-Wyart, and D. Quéré. *Capillarity and Wetting Phenomena*. New York, NY: Springer New York, 2004.
- [37] F. De Goes, C. Wallez, J. Huang, D. Pavlov, and M. Desbrun. “Power Particles: An Incompressible Fluid Solver Based on Power Diagrams”. *ACM Trans. Graph.* 34.4 (2015), pp. 1–11. DOI: 10.1145/2766901.
- [38] F. De Gournay, J. Kahn, and L. Lebrat. “Differentiation and Regularity of Semi-Discrete Optimal Transport with Respect to the Parameters of the Discrete Measure”. *Numer. Math.* 141.2 (2019), pp. 429–453. DOI: 10.1007/s00211-018-1000-4.
- [39] G. De Philippis and A. Figalli. “The Monge–Ampère Equation and Its Link to Optimal Transportation”. *Bull. Amer. Math. Soc.* 51.4 (2014), pp. 527–580. DOI: 10.1090/S0273-0979-2014-01459-4.
- [40] P. Degond, A. Frouvelle, and S. Merino-Aceituno. “A New Flocking Model through Body Attitude Coordination”. *Math. Models Methods Appl. Sci.* 27.06 (2017), pp. 1005–1049. DOI: 10.1142/S0218202517400085.
- [41] A. Diez. “SiSyPHE: A Python Package for the Simulation of Systems of Interacting Mean-Field Particles with High Efficiency”. *Journal of Open Source Software* 6.65 (2021), p. 3653. DOI: 10.21105/joss.03653.

- [42] R. Farhadifar, J.-C. Röper, B. Aigouy, S. Eaton, and F. Jülicher. “The Influence of Cell Mechanics, Cell-Cell Interactions, and Proliferation on Epithelial Packing”. *Current Biology* 17.24 (2007), pp. 2095–2104. DOI: 10.1016/j.cub.2007.11.049.
- [43] J. Feydy. “Geometric Data Analysis, beyond Convolutions”. PhD thesis. Université Paris-Saclay, 2020.
- [44] J. Feydy, B. Charlier, F.-X. Vialard, and G. Peyré. “Optimal Transport for Diffeomorphic Registration”. In: *Medical Image Computing and Computer Assisted Intervention*. MICCAI 2017: 20th International Conference. Quebec city, QC, Canada: Springer, 2017, pp. 291–299.
- [45] J. Feydy, J. Glaunès, B. Charlier, and M. Bronstein. “Fast Geometric Learning with Symbolic Matrices”. In: *Advances in Neural Information Processing Systems*. NeurIPS 2020. Vol. 33. Curran Associates, Inc., 2020, pp. 14448–14462. URL: https://proceedings.neurips.cc/paper_files/paper/2020/file/a6292668b36ef412fa3c4102d1311a62-Paper.pdf.
- [46] J. Feydy, T. Séjourné, F.-X. Vialard, S.-i. Amari, A. Trounev, and G. Peyré. “Interpolating between Optimal Transport and MMD Using Sinkhorn Divergences”. In: *Proceedings of the Twenty-Second International Conference on Artificial Intelligence and Statistics*. The 22nd International Conference on Artificial Intelligence and Statistics. PMLR, 2019, pp. 2681–2690. URL: <https://proceedings.mlr.press/v89/feydy19a.html> (visited on 05/08/2023).
- [47] T. O. Gallouët and Q. Mérigot. “A Lagrangian Scheme à La Brenier for the Incompressible Euler Equations”. *Foundations of Computational Mathematics* 18.4 (2018), pp. 835–865. DOI: 10.1007/s10208-017-9355-y.
- [48] W. Gangbo and R. J. McCann. “The Geometry of Optimal Transportation”. *Acta Math.* 177.2 (1996), pp. 113–161. DOI: 10.1007/BF02392620.
- [49] A. Ghaffarizadeh, R. Heiland, S. H. Friedman, S. M. Mumenthaler, and P. Macklin. “PhysiCell: An Open Source Physics-Based Cell Simulator for 3-D Multicellular Systems”. *PLoS Comput. Biol.* 14.2 (2018). Ed. by T. Poisot, e1005991. DOI: 10.1371/journal.pcbi.1005991.
- [50] J. A. Glazier and F. Graner. “Simulation of the Differential Adhesion Driven Rearrangement of Biological Cells”. *Phys. Rev. E* 47.3 (1993), pp. 2128–2154. DOI: 10.1103/PhysRevE.47.2128.
- [51] B. González-Bermúdez, G. V. Guinea, and G. R. Plaza. “Advances in Micropipette Aspiration: Applications in Cell Biomechanics, Models, and Extended Studies”. *Biophysical Journal* 116.4 (2019), pp. 587–594. DOI: 10.1016/j.bpj.2019.01.004.
- [52] D. S. Goodsell. “Inside a Living Cell”. *Trends in Biochemical Sciences* 16 (1991), pp. 203–206. DOI: 10.1016/0968-0004(91)90083-8.

- [53] F. Graner and J. A. Glazier. “Simulation of Biological Cell Sorting Using a Two-Dimensional Extended Potts Model”. *Phys. Rev. Lett.* 69.13 (1992), pp. 2013–2016. DOI: 10.1103/PhysRevLett.69.2013.
- [54] R. Großmann, I. S. Aranson, and F. Peruani. “A Particle-Field Approach Bridges Phase Separation and Collective Motion in Active Matter”. *Nature Communications* 11.1 (2020), p. 5365. DOI: 10.1038/s41467-020-18978-5.
- [55] K. Guevorkian and J.-L. Maître. “Micropipette Aspiration: A Unique Tool for Exploring Cell and Tissue Mechanics in Vivo”. In: *Methods in Cell Biology*. Ed. by T. Lecuit. Vol. 139. Academic Press, 2017, pp. 187–201.
- [56] C. R. Harris, K. J. Millman, S. J. van der Walt, R. Gommers, P. Virtanen, D. Cournapeau, E. Wieser, J. Taylor, S. Berg, N. J. Smith, R. Kern, M. Picus, S. Hoyer, M. H. van Kerkwijk, M. Brett, A. Haldane, J. F. del Río, M. Wiebe, P. Peterson, P. Gérard-Marchant, K. Sheppard, T. Reddy, W. Weckesser, H. Abbasi, C. Gohlke, and T. E. Oliphant. “Array Programming with NumPy”. *Nature* 585.7825 (2020), pp. 357–362.
- [57] T. Hayashi, T. Tomomizu, T. Sushida, M. Akiyama, S.-I. Ei, and M. Sato. “Tiling Mechanisms of the Drosophila Compound Eye through Geometrical Tessellation”. *Current Biology* 32.9 (2022), 2101–2109.e5. DOI: 10.1016/j.cub.2022.03.046.
- [58] T. Heck, D. A. Vargas, B. Smeets, H. Ramon, P. Van Liedekerke, and H. Van Oosterwyck. “The Role of Actin Protrusion Dynamics in Cell Migration through a Degradable Viscoelastic Extracellular Matrix: Insights from a Computational Model”. *PLoS Comput. Biol.* 16.1 (2020). Ed. by R. M. Merks, e1007250. DOI: 10.1371/journal.pcbi.1007250.
- [59] T. Hiraiwa, K. Shitara, and T. Ohta. “Dynamics of a Deformable Self-Propelled Particle in Three Dimensions”. *Soft Matter* 7.7 (2011), pp. 3083–3086. DOI: 10.1039/C0SM00856G.
- [60] H. Honda. “Description of Cellular Patterns by Dirichlet Domains: The Two-Dimensional Case”. *J. Theoret. Biol.* 72.3 (1978), pp. 523–543. DOI: 10.1016/0022-5193(78)90315-6.
- [61] H. Honda, M. Tanemura, and T. Nagai. “A Three-Dimensional Vertex Dynamics Cell Model of Space-Filling Polyhedra Simulating Cell Behavior in a Cell Aggregate”. *J. Theoret. Biol.* 226.4 (2004), pp. 439–453. DOI: 10.1016/j.jtbi.2003.10.001.
- [62] J. D. Hunter. “Matplotlib: A 2D Graphics Environment”. *Comput. Sci. Eng.* 9.3 (2007), pp. 90–95.

- [63] S. Ichbiah, F. Delbary, A. McDougall, R. Dumollard, and H. Turlier. “Embryo Mechanics Cartography: Inference of 3D Force Atlases from Fluorescence Microscopy”. *Nat. Methods* 20.12 (2023), pp. 1989–1999. DOI: 10.1038/s41592-023-02084-7.
- [64] T. Ichikawa, H. T. Zhang, L. Panavaite, A. Erzberger, D. Fabrèges, R. Snajder, A. Wolny, E. Korotkevich, N. Tsuchida-Straeten, L. Hufnagel, A. Kreshuk, and T. Hiiragi. “An Ex Vivo System to Study Cellular Dynamics Underlying Mouse Peri-Implantation Development”. *Developmental Cell* 57.3 (2022), 373–386.e9. DOI: 10.1016/j.devcel.2021.12.023.
- [65] Y. Ishimoto and Y. Morishita. “Bubbly Vertex Dynamics: A Dynamical and Geometrical Model for Epithelial Tissues with Curved Cell Shapes”. *Phys. Rev. E* 90.5 (2014), p. 052711. DOI: 10.1103/PhysRevE.90.052711.
- [66] P.-E. Jabin and Z. Wang. “Mean Field Limit for Stochastic Particle Systems”. In: *Active Particles, Volume 1 : Advances in Theory, Models, and Applications*. Ed. by N. Bellomo, P. Degond, and E. Tadmor. Modeling and Simulation in Science, Engineering and Technology. Birkhäuser Basel, 2017, pp. 379–402. DOI: 10.1007/978-3-319-49996-3_10.
- [67] Y. Jamali, M. Azimi, and M. R. K. Mofrad. “A Sub-Cellular Viscoelastic Model for Cell Population Mechanics”. *PLoS ONE* 5.8 (2010). Ed. by N. Monk, e12097. DOI: 10.1371/journal.pone.0012097.
- [68] G. T. Johnson, L. Autin, M. Al-Alusi, D. S. Goodsell, M. F. Sanner, and A. J. Olson. “cellPACK: A Virtual Mesoscope to Model and Visualize Structural Systems Biology”. *Nature Methods* 12.1 (2015), pp. 85–91. DOI: 10.1038/nmeth.3204.
- [69] M. Kac. “Foundations of Kinetic Theory”. In: *Proceedings of the Third Berkeley Symposium on Mathematical Statistics and Probability*. Vol. 3. University of California Press Berkeley and Los Angeles, California, 1956, pp. 171–197.
- [70] S. Kachalo, H. Naveed, Y. Cao, J. Zhao, and J. Liang. “Mechanical Model of Geometric Cell and Topological Algorithm for Cell Dynamics from Single-Cell to Formation of Monolayered Tissues with Pattern”. *PLOS ONE* 10.5 (2015). Ed. by R. M. Merks, e0126484. DOI: 10.1371/journal.pone.0126484.
- [71] S. Kaliman, C. Jayachandran, F. Rehfeldt, and A.-S. Smith. “Limits of Applicability of the Voronoi Tessellation Determined by Centers of Cell Nuclei to Epithelium Morphology”. *Front. Physiol.* 7 (2016). DOI: 10.3389/fphys.2016.00551.

- [72] F. N. Kenny, S. Marcotti, D. B. De Freitas, E. M. Drudi, V. Leech, R. E. Bell, J. Easton, M.-d.-C. Díaz-de-la Loza, R. Fleck, L. Allison, C. Philippeos, A. Manhart, T. J. Shaw, and B. M. Stramer. “Autocrine IL-6 Drives Cell and Extracellular Matrix Anisotropy in Scar Fibroblasts”. *Matrix Biology* 123 (2023), pp. 1–16. DOI: 10.1016/j.matbio.2023.08.004.
- [73] J. Kitagawa, Q. Mérigot, and B. Thibert. “Convergence of a Newton Algorithm for Semi-Discrete Optimal Transport”. *J. Eur. Math. Soc.* 21.9 (2019), pp. 2603–2651. DOI: 10.4171/JEMS/889.
- [74] X. Kuang, G. Guan, C. Tang, and L. Zhang. “MorphoSim: An Efficient and Scalable Phase-Field Framework for Accurately Simulating Multicellular Morphologies”. *npj Systems Biology and Applications* 9.1 (2023), p. 6. DOI: 10.1038/s41540-023-00265-w.
- [75] D. A. Kulawiak, B. A. Camley, and W.-J. Rappel. “Modeling Contact Inhibition of Locomotion of Colliding Cells Migrating on Micropatterned Substrates”. *PLoS Comput. Biol.* 12.12 (2016). Ed. by P. K. Maini, e1005239. DOI: 10.1371/journal.pcbi.1005239.
- [76] H. Leclerc, Q. Mérigot, F. Santambrogio, and F. Stra. “Lagrangian Discretization of Crowd Motion and Linear Diffusion”. *SIAM J. Numer. Anal.* 58.4 (2020), pp. 2093–2118. DOI: 10.1137/19M1274201.
- [77] T. Lecuit and P.-F. Lenne. “Cell Surface Mechanics and the Control of Cell Shape, Tissue Patterns and Morphogenesis”. *Nat. Rev. Mol. Cell Biol.* 8.8 (2007), pp. 633–644. DOI: 10.1038/nrm2222.
- [78] V. Leech, F. N. Kenny, S. Marcotti, T. J. Shaw, B. M. Stramer, and A. Manhart. “Derivation and Simulation of a Computational Model of Active Cell Populations: How Overlap Avoidance, Deformability, Cell-Cell Junctions and Cytoskeletal Forces Affect Alignment”. *bioRxiv preprint* (2024). DOI: 10.1101/2024.02.02.578535.
- [79] B. Levy, R. Mohayaee, and S. von Hausegger. “A Fast Semidiscrete Optimal Transport Algorithm for a Unique Reconstruction of the Early Universe”. *Monthly Notices of the Royal Astronomical Society* 506.1 (2021), pp. 1165–1185. DOI: 10.1093/mnras/stab1676.
- [80] B. Lévy. *Geogram*. GitHub repository. URL: <https://github.com/BrunoLevy/geogram>.
- [81] B. Lévy. “Partial Optimal Transport for a Constant-Volume Lagrangian Mesh with Free Boundaries”. *J. Comput. Phys.* 451 (2022), p. 110838. DOI: 10.1016/j.jcp.2021.110838.
- [82] B. Lévy and Y. Liu. “ L_p Centroidal Voronoi Tessellation and Its Applications”. *ACM Trans. Graph.* 29.4 (2010), pp. 1–11. DOI: 10.1145/1778765.1778856.

- [83] P. Madhikar, J. Åström, J. Westerholm, and M. Karttunen. “CellSim3D: GPU Accelerated Software for Simulations of Cellular Growth and Division in Three Dimensions”. *Computer Physics Communications* 232 (2018), pp. 206–213. DOI: 10.1016/j.cpc.2018.05.024.
- [84] E. Mansfield, H. Sepangi, and E. Eastwood. “Equilibrium and Mutual Attraction or Repulsion of Objects Supported by Surface Tension”. *Philosophical Transactions: Mathematical, Physical and Engineering Sciences* 335.1726 (1997), pp. 869–919.
- [85] B. Maury, A. Roudneff-Chupin, F. Santambrogio, and J. Venel. “Handling Congestion in Crowd Motion Modeling”. *Networks & Heterogeneous Media* 6.3 (2011), pp. 485–519. DOI: 10.3934/nhm.2011.6.485.
- [86] J.-L. Maître, H. Berthoumieux, S. F. G. Krens, G. Salbreux, F. Jülicher, E. Paluch, and C.-P. Heisenberg. “Adhesion Functions in Cell Sorting by Mechanically Coupling the Cortices of Adhering Cells”. *Science* 338.6104 (2012), pp. 253–256. DOI: 10.1126/science.1225399.
- [87] H. P. McKean. “Propagation of Chaos for a Class of Non-Linear Parabolic Equations”. In: *Lecture Series in Differential Equations, Volume 2*. Ed. by A. K. Aziz. Van Nostrand Mathematical Studies 19. Van Nostrand Reinhold Company, 1969, pp. 177–194.
- [88] S. Megason, D. Oo, K. Konstantinopoulos, M. Mitsch, D. Willis, A. Almaghasilah, A. Ruzette, V. Bidhan, J. De Man, N. Lin, J. Gui, and R. Gowani. *Goo Is a Python-based Blender Extension for Modeling Biological Cells, Tissues, and Embryos*. Version v0.0.1-beta1. GitHub repository, 2023. DOI: 10.5281/ZENODO.10296203.
- [89] Q. Merigot and H. Leclerc. *Pysdot*. GitHub repository. URL: <https://github.com/sd-ot/pysdot>.
- [90] Q. Merigot, F. Santambrogio, and C. Sarrazin. “Non-Asymptotic Convergence Bounds for Wasserstein Approximation Using Point Clouds”. In: *Advances in Neural Information Processing Systems*. NeurIPS 2021. Vol. 34. Curran Associates, Inc., 2021, pp. 12810–12821. URL: https://proceedings.neurips.cc/paper_files/paper/2021/file/6a61d423d02a1c56250dc23ae7ff12f3-Paper.pdf.
- [91] J. Meyron. *Sdot*. GitHub repository. URL: <https://github.com/nyorem/sdot>.
- [92] S. Miyazaki, T. Otani, K. Sugihara, T. Fujimori, M. Furuse, and T. Miura. “Mechanism of Interdigitation Formation at Apical Boundary of MDCK Cell”. *iScience* 26.5 (2023), p. 106594. DOI: 10.1016/j.isci.2023.106594.

- [93] P. Moghe, R. Belousov, T. Ichikawa, C. Iwatani, T. Tsukiyama, F. Graner, A. Erzberger, and T. Hiiragi. “Apical-Driven Cell Sorting Optimised for Tissue Geometry Ensures Robust Patterning”. *Preprint* (2023). DOI: 10.1101/2023.05.16.540918.
- [94] R. Z. Mohammad, H. Murakawa, K. Svadlenka, and H. Togashi. “A Numerical Algorithm for Modeling Cellular Rearrangements in Tissue Morphogenesis”. *Commun. Biol.* 5.1 (2022), p. 239. DOI: 10.1038/s42003-022-03174-6.
- [95] F. Mugele and J. Heikenfeld. *Electrowetting: Fundamental Principles and Practical Applications*. Weinheim: Wiley-VCH, 2019.
- [96] E. Méhes and T. Vicsek. “Collective Motion of Cells: From Experiments to Models”. *Integr. Biol.* 6.9 (2014), pp. 831–854. DOI: 10.1039/C4IB00115J.
- [97] S. Méléard. “Asymptotic Behaviour of Some Interacting Particle Systems; McKean-Vlasov and Boltzmann Models”. In: *Probabilistic Models for Non-linear Partial Differential Equations*. Ed. by D. Talay and L. Tubaro. Lecture Notes in Mathematics 1627. Springer-Verlag Berlin Heidelberg, 1996.
- [98] Q. Mérigot. “A Multiscale Approach to Optimal Transport”. In: *Computer Graphics Forum*. Vol. 30. 5. Wiley Online Library, 2011, pp. 1583–1592.
- [99] M. Nagayama, H. Monobe, K. Sakakibara, K.-I. Nakamura, Y. Kobayashi, and H. Kitahata. “On the Reaction–Diffusion Type Modelling of the Self-Propelled Object Motion”. *Scientific Reports* 13.1 (2023), p. 12633. DOI: 10.1038/s41598-023-39395-w.
- [100] A. Natale. “Gradient Flows of Interacting Laguerre Cells as Discrete Porous Media Flows”. 2023. arXiv: 2304.05069.
- [101] M. Nonomura. “Study on Multicellular Systems Using a Phase Field Model”. *PLoS ONE* 7.4 (2012), e33501. DOI: 10.1371/journal.pone.0033501.
- [102] Nvidia. *NVIDIA Omniverse™*. URL: <https://developer.nvidia.com/omniverse>.
- [103] T. Ohta. “Dynamics of Deformable Active Particles”. *Journal of the Physical Society of Japan* 86.7 (2017), p. 072001. DOI: 10.7566/JPSJ.86.072001.
- [104] T. Ohta, T. Ohkuma, and K. Shitara. “Deformation of a Self-Propelled Domain in an Excitable Reaction-Diffusion System”. *Physical Review E* 80.5 (2009), p. 056203. DOI: 10.1103/PhysRevE.80.056203.
- [105] J. M. Osborne, A. G. Fletcher, J. M. Pitt-Francis, P. K. Maini, and D. J. Gavaghan. “Comparing Individual-Based Approaches to Modelling the Self-Organization of Multicellular Tissues”. *PLoS Comput. Biol.* 13.2 (2017). Ed. by Q. Nie, e1005387. DOI: 10.1371/journal.pcbi.1005387.

- [106] S. Osher and R. Fedkiw. *Level Set Methods and Dynamic Implicit Surfaces*. Applied Mathematical Sciences 153. New York Berlin Heidelberg: Springer, 2003. 273 pp.
- [107] S. Osher and J. A. Sethian. “Fronts Propagating with Curvature-Dependent Speed: Algorithms Based on Hamilton-Jacobi Formulations”. *J. Comput. Phys.* 79.1 (1988), pp. 12–49. DOI: 10.1016/0021-9991(88)90002-2.
- [108] A. Paszke, S. Gross, F. Massa, A. Lerer, J. Bradbury, G. Chanan, T. Killeen, Z. Lin, N. Gimelshein, L. Antiga, A. Desmaison, A. Kopf, E. Yang, Z. DeVito, M. Raison, A. Tejani, S. Chilamkurthy, B. Steiner, L. Fang, J. Bai, and S. Chintala. “PyTorch: An Imperative Style, High-Performance Deep Learning Library”. In: *Advances in Neural Information Processing Systems*. NeurIPS 2019. Ed. by H. Wallach, H. Larochelle, A. Beygelzimer, F. Alché-Buc, E. Fox, and R. Garnett. Vol. 32. Curran Associates, Inc., 2019. URL: <https://proceedings.neurips.cc/paper/2019/file/bdbca288fee7f92f2bfa9f70127277Paper.pdf>.
- [109] C. S. Peskin. “The Immersed Boundary Method”. *Acta Numerica* 11 (2002), pp. 479–517. DOI: 10.1017/S0962492902000077.
- [110] G. Peyré and M. Cuturi. “Computational Optimal Transport: With Applications to Data Science”. *Foundations and Trends® in Machine Learning* 11.5-6 (2019), pp. 355–607. DOI: 10.1561/22000000073.
- [111] S. Plunder and S. Merino-Aceituno. “Convergence Proof for First-Order Position-Based Dynamics: An Efficient Scheme for Inequality Constrained ODEs”. 2023. arXiv: 2310.01215. URL: <http://arxiv.org/abs/2310.01215>.
- [112] Z. Qu, M. Li, F. De Goes, and C. Jiang. “The Power Particle-in-Cell Method”. *ACM Transactions on Graphics* 41.4 (2022).
- [113] Z. Qu, M. Li, Y. Yang, C. Jiang, and F. De Goes. “Power Plastics: A Hybrid Lagrangian/Eulerian Solver for Mesoscale Inelastic Flows”. *ACM Transactions on Graphics* 42.6 (2023), pp. 1–11.
- [114] I. Quilez. *Raymarching Primitives*. 2013. URL: <https://iquilezles.org/articles/distfunctions/>.
- [115] N. Ray, D. Sokolov, S. Lefebvre, and B. Lévy. “Meshless Voronoi on the GPU”. *ACM Transactions on Graphics* 37.6 (2018), pp. 1–12.
- [116] K. A. Rejniak. “An Immersed Boundary Framework for Modelling the Growth of Individual Cells: An Application to the Early Tumour Development”. *J. Theoret. Biol.* 247.1 (2007), pp. 186–204. DOI: 10.1016/j.jtbi.2007.02.019.

- [117] S. Runser, R. Vetter, and D. Iber. “SimuCell3D: Three-Dimensional Simulation of Tissue Mechanics with Cell Polarization”. *Nat. Comput. Sci.* (2024). DOI: 10.1038/s43588-024-00620-9.
- [118] N. Saito and S. Ishihara. “Active Deformable Cells Undergo Cell Shape Transition Associated with Percolation of Topological Defects”. 2023. arXiv: 2303.03580.
- [119] F. Santambrogio. *Optimal Transport for Applied Mathematicians: Calculus of Variations, PDEs, and Modeling*. Vol. 87. Progress in Nonlinear Differential Equations and Their Applications. Springer International Publishing, 2015. DOI: 10.1007/978-3-319-20828-2.
- [120] C. Sarrazin. “Lagrangian Discretization of Variational Mean Field Games”. *SIAM J. Control Optim.* 60.3 (2022), pp. 1365–1392. DOI: 10.1137/20M1377291.
- [121] R. I. Saye and J. A. Sethian. “The Voronoi Implicit Interface Method for Computing Multiphase Physics”. *Proc. Natl. Acad. Sci. U.S.A.* 108.49 (2011), pp. 19498–19503. DOI: 10.1073/pnas.1111557108.
- [122] G. Schiebinger, J. Shu, M. Tabaka, B. Cleary, V. Subramanian, A. Solomon, J. Gould, S. Liu, S. Lin, P. Berube, et al. “Optimal-Transport Analysis of Single-Cell Gene Expression Identifies Developmental Trajectories in Reprogramming”. *Cell* 176.4 (2019), pp. 928–943.
- [123] B. Schmitzer. “A Sparse Multiscale Algorithm for Dense Optimal Transport”. *J. Math. Imaging Vision* 56 (2016), pp. 238–259.
- [124] B. Schmitzer. “Stabilized Sparse Scaling Algorithms for Entropy Regularized Transport Problems”. *SIAM J. Sci. Comput.* 41.3 (2019), A1443–A1481.
- [125] T. J. Seigo, T. Comlekoglu, S. M. Peirce, D. W. Desimone, and J. A. Glazier. “General, Open-Source Vertex Modeling in Biological Applications Using Tissue Forge”. *Scientific Reports* 13.1 (2023), p. 17886. DOI: 10.1038/s41598-023-45127-x.
- [126] S. Seirin-Lee, K. Yamamoto, and A. Kimura. “The Extra-Embryonic Space and the Local Contour Are Crucial Geometric Constraints Regulating Cell Arrangement”. *Development* 149.9 (2022), dev200401. DOI: 10.1242/dev.200401.
- [127] S. SenGupta, C. A. Parent, and J. E. Bear. “The Principles of Directed Cell Migration”. *Nat. Rev. Mol. Cell Biol.* 22.8 (2021), pp. 529–547. DOI: 10.1038/s41580-021-00366-6.
- [128] J. A. Sethian. *Level Set Methods and Fast Marching Methods: Evolving Interfaces in Computational Geometry, Fluid Mechanics, Computer Vision, and Materials Science*. 2nd ed. Cambridge Monographs on Applied and Computational Mathematics 3. Cambridge, U.K. ; New York: Cambridge University Press, 1999. 378 pp.

- [129] H. Shafqat-Abbasi, J. M. Kowalewski, A. Kiss, X. Gong, P. Hernandez-Varas, U. Berge, M. Jafari-Mamaghani, J. G. Lock, and S. Strömlad. “An Analysis Toolbox to Explore Mesenchymal Migration Heterogeneity Reveals Adaptive Switching between Distinct Modes”. *eLife* 5.e11384 (2016). DOI: 10.7554/eLife.11384.
- [130] Z. Shen, J. Feydy, P. Liu, A. H. Curiale, R. San Jose Estepar, R. San Jose Estepar, and M. Niethammer. “Accurate Point Cloud Registration with Robust Optimal Transport”. In: *Advances in Neural Information Processing Systems*. NeurIPS 2021. Vol. 34. Curran Associates, Inc., 2021, pp. 5373–5389.
- [131] A. Song. “Generation of Tubular and Membranous Shape Textures with Curvature Functionals”. *J. Math. Imaging Vision* 64.1 (2022), pp. 17–40.
- [132] J. Starruß, W. De Back, L. Brusch, and A. Deutsch. “Morpheus: A User-Friendly Modeling Environment for Multiscale and Multicellular Systems Biology”. *Bioinformatics* 30.9 (2014), pp. 1331–1332. DOI: 10.1093/bioinformatics/btt772.
- [133] C Sullivan and A. Kaszynski. “PyVista: 3D Plotting and Mesh Analysis through a Streamlined Interface for the Visualization Toolkit (VTK)”. *Journal of Open Source Software* 4.37 (2019), p. 1450.
- [134] D. Sulsky, S. Childress, and J. Percus. “A Model of Cell Sorting”. *J. Theoret. Biol.* 106.3 (1984), pp. 275–301. DOI: 10.1016/0022-5193(84)90031-6.
- [135] M. H. Swat, G. L. Thomas, J. M. Belmonte, A. Shirinifard, D. Hmeljak, and J. A. Glazier. “Multi-Scale Modeling of Tissues Using CompuCell3D”. In: *Methods in Cell Biology*. Vol. 110. Elsevier, 2012, pp. 325–366.
- [136] J.-M. Swiecicki, O. Sliusarenko, and D. B. Weibel. “From Swimming to Swarming: Escherichia Coli Cell Motility in Two-Dimensions”. *Integr. Biol.* 5.12 (2013), p. 1490. DOI: 10.1039/c3ib40130h.
- [137] A.-S. Sznitman. “Topics in Propagation of Chaos”. In: *Éc. Été Probab. St.-Flour XIX—1989*. Springer, 1991, pp. 165–251.
- [138] H. Togashi, K. Kominami, M. Waseda, H. Komura, J. Miyoshi, M. Takeichi, and Y. Takai. “Nectins Establish a Checkerboard-Like Cellular Pattern in the Auditory Epithelium”. *Science* 333.6046 (2011), pp. 1144–1147. DOI: 10.1126/science.1208467.
- [139] A. Torres-Sánchez, M. Kerr Winter, and G. Salbreux. “Interacting Active Surfaces: A Model for Three-Dimensional Cell Aggregates”. *PLoS Comput. Biol.* 18.12 (2022). Ed. by S. Ares, e1010762. DOI: 10.1371/journal.pcbi.1010762.
- [140] H. Turlier and J.-L. Maître. “Mechanics of Tissue Compaction”. *Semin. Cell Dev. Biol.* 47–48 (2015), pp. 110–117. DOI: 10.1016/j.semcdb.2015.08.001.

- [141] P. Van Liedekerke, M. M. Palm, N. Jagiella, and D. Drasdo. “Simulating Tissue Mechanics with Agent-Based Models: Concepts, Perspectives and Some Novel Results”. *Computational Particle Mechanics* 2.4 (2015), pp. 401–444. DOI: 10.1007/s40571-015-0082-3.
- [142] R. Vetter, S. V. Runser, and D. Iber. “PolyHoop: Soft Particle and Tissue Dynamics with Topological Transitions”. *Computer Physics Communications* 299 (2024), p. 109128. DOI: 10.1016/j.cpc.2024.109128.
- [143] T. Vicsek, A. Czirók, E. Ben-Jacob, I. Cohen, and O. Shochet. “Novel Type of Phase Transition in a System of Self-Driven Particles”. *Phys. Rev. Lett.* 75.6 (1995), pp. 1226–1229. DOI: 10.1103/PhysRevLett.75.1226.
- [144] T. Vicsek and A. Zafeiris. “Collective Motion”. *Phys. Rep.* 517.3-4 (2012), pp. 71–140. DOI: 10.1016/j.physrep.2012.03.004.
- [145] C. Villani. *Topics in Optimal Transportation*. Graduate Studies in Mathematics 58. American Mathematical Society, 2003. 370 pp.
- [146] C. Villani. *Optimal Transport, Old and New*. Grundlehren Der Mathematischen Wissenschaften 338. Springer-Verlag Berlin Heidelberg, 2009. DOI: 10.1007/978-3-540-71050-9.
- [147] S.-Q. Xin, B. Lévy, Z. Chen, L. Chu, Y. Yu, C. Tu, and W. Wang. “Centroidal Power Diagrams with Capacity Constraints: Computation, Applications, and Extension”. *ACM Transactions on Graphics* 35.6 (2016), pp. 1–12. DOI: 10.1145/2980179.2982428.
- [148] L. Yang, J. C. Effler, B. L. Kutscher, S. E. Sullivan, D. N. Robinson, and P. A. Iglesias. “Modeling Cellular Deformations Using the Level Set Formalism”. *BMC Syst. Biol.* 2.1 (2008), p. 68. DOI: 10.1186/1752-0509-2-68.
- [149] J. Zhao, Y. Cao, L. A. DiPietro, and J. Liang. “Dynamic Cellular Finite-Element Method for Modelling Large-Scale Cell Migration and Proliferation under the Control of Mechanical and Biochemical Cues: A Study of Re-Epithelialization”. *J. R. Soc. Interface.* 14.129 (2017), p. 20160959. DOI: 10.1098/rsif.2016.0959.